Master Thesis

Transport properties of stacked Josephson junctions employing Permalloy ferromagnetic barrier

Department of Physics "Ettore Pacini"
University of Naples Federico II

Supervisors:
Prof. Francesco Tafuri
Dr. Domenico Montemurro

Candidate:
Paola Savarese
Matr.:N94/562

Academic Year 2021/2022

Introduction

Josephson junctions (JJs) are characterized by high switching speed, low power dissipation and the ability to interconnect superconducting lines with low dispersion, without losses. Thanks to their properties, JJs are of great interest to different applications: ranging from sensor applications, even in the quantum limit, to key components of superconducting quantum processors used in quantum computers [1][2] [3].
Single-flux quantum (SFQ) logic is widely used in superconducting JJs technology and is characterized by low switching energy and high switching speed, but its applications are still limited due to the low integration density and the lack of a high-capacity cryogenic memory compatible with SFQ logic, in terms of speed and power dissipation [4]. The use of devices combining ferromagnets and superconductors represents a promising approach for the realization of integrated memories for superconducting circuits [3]. SFS (Superconductor-Ferromagnet-Superconductor) JJs have been mostly used as passive elements in superconducting circuits and have not been considered so far in the realization of quantum circuits because they exhibit high quasiparticle dissipation, which results from the metallic nature of the usual ferromagnetic barriers. Advances in coupling ferromagnetic layers with insulating barriers within the JJs (SIsFS or SIFS JJs) and the ability to use intrinsic insulating ferromagnetic materials allow us to develop ferromagnetic JJs characterized by high-quality factors and low quasiparticle losses [5].
With the aim of highlighting the main characteristics of a SIsFS (Superconductor-Insulator-ThinSuperconductor-Ferromagnet-Superconductor) JJ, in this thesis work, two different types of Josephson junctions were compared: the first without ferromagnet; the second with a layer of ferromagnetic material, Permalloy.
Originally realized on Nb, the ferromagnetic junctions are extended to Al, which is the technology most used for all quantum circuits and processors. The results are encouraging and support the idea that these junctions can be used in quantum architectures.

This thesis is developed as follow: chapter 1 - the introduction to the theory inherent to Josephson junctions and the need to understand the experimental results are discussed; chapter 2 - the fabrication process as well as notions on the used fabrication techniques useful to investigate the devices object of this thesis are discussed; chapter 3 - is dedicated to the description of the used 10mK refrigerator and to the measurements setup; last chapter of this thesis work reports on the data analysis and the discussion of the collected results.

Contents

List of Figures

List of Tables

Chapter 1

General aspects

1.1 Introduction to superconductivity

The discovery of superconductivity took place in 1911 by Kamerling Onnes, at the Leiden laboratories. Onnes was conducting experiments using a mercury sample, measuring resistance as a function of temperature, in figure 1.1, he observed that for temperature values lower than those of the critical temperature, T_c, (for Hg is 4.20 K [6]), the resistance vanished sharply. Because of that, superconducting ma-

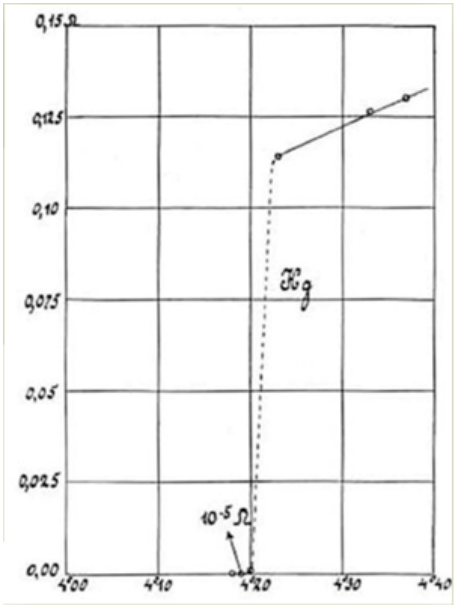

Figure 1.1: Historic plot of resistance versus temperature for mercury measurement carried out on October 26 th 1911. It shows the superconducting transition at 4.20 K for Hg. Within 0.01 K of accuracy, the resistance jumps from unmeasurably small value (less than $10^{-6}\Omega$) to 0.1 Ω [6].

terials behave as a normal conductor for temperature higher than T_c and, as the temperature decreases, in correspondence of the T_c, they undergo a transition to a new state, the *superconducting state*, in which the resistance is zero [7].

An experimental confirm of the existence of the superconducting state is shown figure 1.2. Here the heat capacity is proportional to the temperature in the normal regime, instead at the superconducting transition it shows a discontinuous, while

at low temperatures it varies as $e^{-\frac{\Delta}{kT_c}}$ [6]. In addition to having zero resistivity for

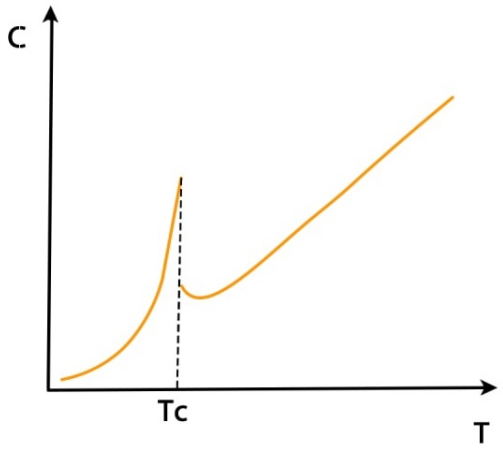

Figure 1.2: Temperature dependence of the heat capacity for a superconducting material.

temperature below T_c, superconductors behave like perfect diamagnets, exhibiting the *Meissner effect*: screening currents circulates on the sample surface thus generating a magnetic field with opposite direction to the applied one [6]. If a low amplitude external magnetic field is applied to the superconductor its flux lines are ejected from the material[6] [8]. In figure 1.3 two experiments conducted on a perfect diamagnet and on a superconductor are shown in order to demonstrate that: a superconductor behaves like a perfect diamagnet, but not the other way around [7]. In the first experiment the samples are cooled and then a magnetic field is applied.

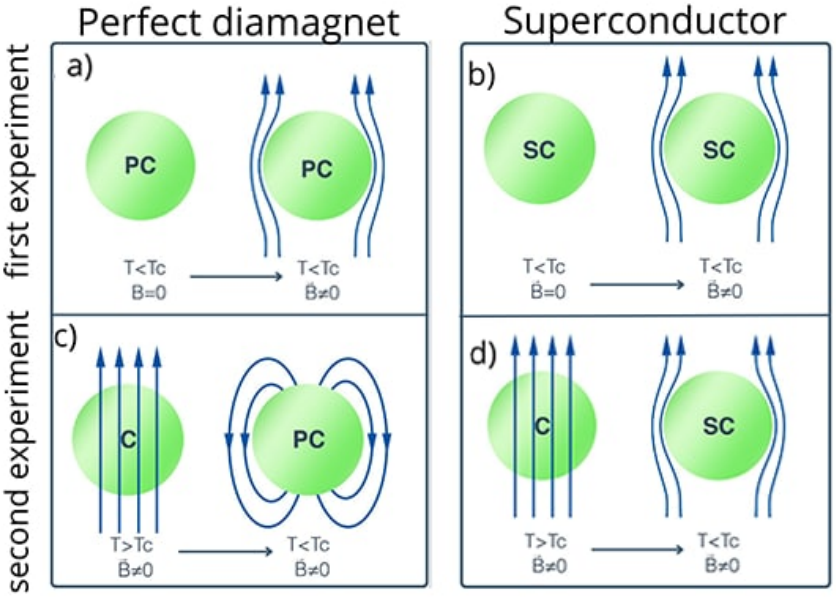

Figure 1.3: The figure shows a comparison between a perfect conductor and superconducting material as a function of the applied magnetic field and the temperature: a)-c) perfect diamagnet material; b)-d) a superconducting material.

Both samples completely expel the magnetic field from the inner part (see fig. 1.3 a) b)). Inside the perfect conductors induced currents shield the flux, while within a superconductor the expulsion of the flux is due to the *Meissner effect*. In the second experiment it is first applied a magnetic field and subsequently the sample is brought to low temperatures (see fig. 1.3 c) d)). It is observed that the superconductor expels the magnetic field lines by the *Meissner effect*, the conductor, on the other hand, is penetrated by the field lines.
These phenomenon give evidence that superconductivity is a real new thermodynamic state and not a consequence of good conductivity [7].

1.1.1 First and second type superconductors

A classification of the superconductors, of the first and second types, is developed by considering their response to an external magnetic field.
The dependence of the critical field on the temperature is given by eq 1.1.

$$H_c(T) = H_c(0)\left[1 - (T/T_c)^2\right] \tag{1.1}$$

where $H_c(0)$ is the extrapolated value of the critical field strength at absolute zero [9].

Taking into account eq.1.1, we can observe that:

- in correspondence of the critical temperature the system shows a magnetic critical field equal to zero;

- by applying an external magnetic field to the superconductor, higher than a threshold value, *critical field*, its normal resistance is restored.

Considering the response to the applied magnetic field of a superconductor, we can distinguish between:
Superconductors of the *first type*
They show a single critical magnetic field (see fig.1.4-a) while the magnetization (see fig.1.4-b) displays a linear dependence on the applied magnetic field. For field values above H_c a phase transition to normal phase takes place otherwise it stays in the superconducting phase [7] [8].

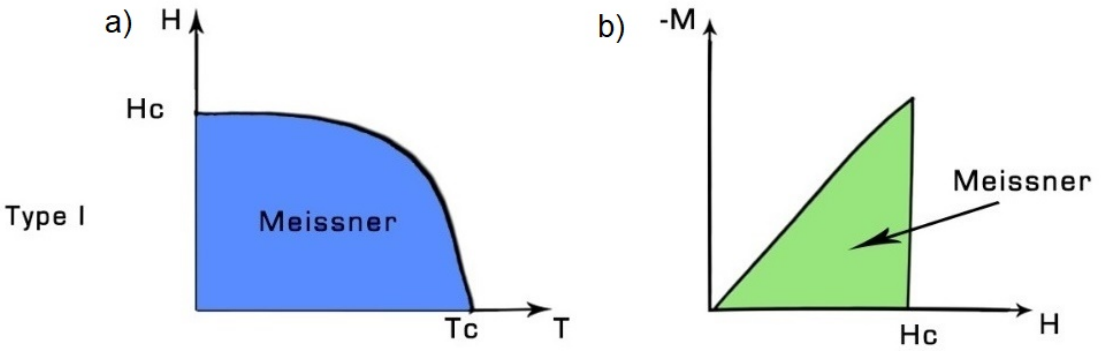

Figure 1.4: It shows for a superconductor of type I- a) the temperature dependence of the magnetic field - b) the dependence of the magnetization on the external magnetic field.

Superconductors of the *second type*
They show a temperature dependences of the magnetic field with two values of critical field: H_{c_1} and H_{c_2} (see fig. 1.5-a). While for applied magnetic field up to H_{c_1} it behaves like first type, for $H_{c_1} < \mathrm{H} < H_{c_2}$ the magnetic field penetrates into material generating a vortices responsible of the dissipation [7]; this phase is called *Mixed state*. For values of $H > H_{c_2}$ it behaves like a normal. Table 1.1 summarizes

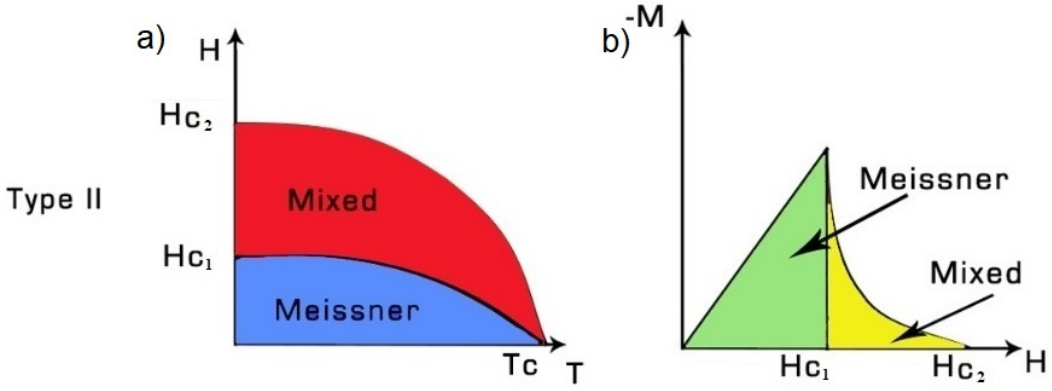

Figure 1.5: It shows for a superconductor of type II- a) the temperature dependence of the magnetic field - b) the dependence of the magnetization on the external magnetic field.

the T_c and H_c for first and second-type superconductors.

Material	**Type**	$H_c(0)$ **(T)**	T_c**(K)**
Ga	first	~ 0.02	1.1
Al	first	~ 0.01	1.2
In	first	~ 0.50	3.4
Hg	first	~ 0.50	4.2
Pb	first	~ 0.10	7.2
Nb	second	~ 170, ~ 240	8.8
NbN	second	~ 20, ~ 240	16.1
YBCO	second	$\sim 250; 120$, ~ 240	94.2

Table 1.1: First and second type superconductors and their critical temperatures and critical magnetic fields [10].

1.2 Theory of superconducting materials

Following it will be briefly introduced models useful to describe the superconducting phase.

1.2.1 London Equation

The first phenomenological model capable of explaining the developments of superconductivity and the Meissner effect was proposed, in 1935, by the brothers F. and H. London [1] [11]. Their idea is based on the *two-fluid model*, according to which,

the density of current flowing inside a superconductor is given by:

$$\vec{J} = \vec{J}_n + \vec{J}_s \tag{1.2}$$

where $\vec{J}_n$ is the *normal density current*, and $\vec{J}_s$ represents the *superconducting density current*. For $T > T_c$, $\vec{J}_n$=σ $\vec{E}$, otherwise $\vec{J}_n$=0 instead $\vec{J}_s = n_s q \vec{v}_s$, where n_s is the superconducting charge density, q is the charge and $\vec{v}_s$is the superconducting velocity.

Applying the equation of motion to the carriers, $m_s\vec{a}$=-q$\vec{E}$, we obtain *the first London equation* 1.3.

$$\frac{d\vec{J}_S}{dt} = \frac{n_S q^2}{m_S}\vec{E} \tag{1.3}$$

that describes the dynamics of electrons in the absence of collisions.

By combining the first London equation with Faraday's law of induction, $\vec{\nabla} \times \vec{E} = -\frac{\partial \vec{B}}{\partial t}$, we can obtain *the second London equation*:

$$\vec{\nabla} \times \vec{J}_S - \frac{n_s q^2}{m_S c}\vec{B} = 0. \tag{1.4}$$

.

By combining the second London equation with Ampere's law, we can obtain an equation for the magnetic field and for the current density:

$$\nabla^2\vec{B} = \tfrac{1}{{\lambda_L}^2}\vec{B} \qquad \text{and} \qquad \nabla^2\vec{J} = \tfrac{1}{{\lambda_L}^2}\vec{J}.$$

with λ_L*London penetration length*

$$\lambda_L = \sqrt{\frac{m_s c^2}{4\pi n_S q^2}} \tag{1.5}$$

where, m_s is the mass, n_s represents the superconducting electron density and q is the charge. The London penetration depth represents the distance in which the magnetic field penetrates inside a superconductor.

The value of the London penetration length depends on the material. In table 1.2 are reported some values of London penetration length.

Metal	**Th. λ_L (nm)**
Al	50
Sn	34
Pb	37
Cd	110
NbN	$\sim$ 200
Nb	44
YBCO	150-300; λ_L^a/1.2; $\sim$ 1000

Table 1.2: London penetration length for bulk materials [10].

λ_L(T) increases slowly at low temperatures and diverges approaching the transition temperature T_c.
The empirical law that predicts the temperature dependence of the London penetration depth is:

$$\lambda_L(T) = \lambda_L(0)\left[1 - \left(\frac{T}{T_c}\right)^4\right]^{-\frac{1}{2}} \tag{1.6}$$

But, if we want to understand what happens when an external magnetic field is applied to a superconductor, we have to consider a three-dimensional space, in which a superconducting material is found for z> 0, the vacuum for z<0 and an external field applied to the superconductor, as shown in figure 1.6. The external magnetic

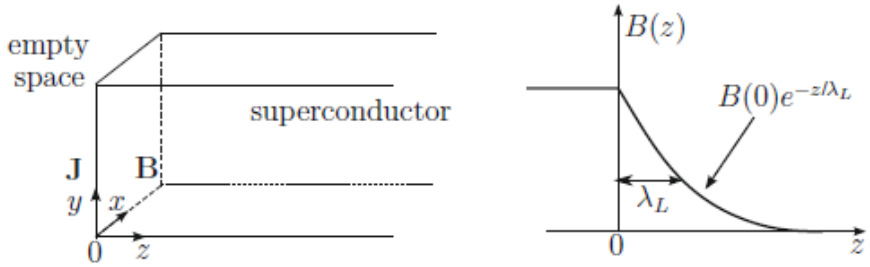

Figure 1.6: On the left, a semi infinite superconducting plate while on the right the penetration depth when the magnetic field is applied along z-direction. Image adapted by [12].

field with a direction orthogonal to the separation surface, cannot penetrate inside the superconductor because the Meissner effect occurs. If the direction of the external magnetic field is parallel to the separation surface, the field penetrates inside the superconductor and decays exponentially, following the behavior: $\vec{B} = \vec{B}_0 e^{-\frac{z}{\lambda_L}}$ [7].

1.2.2 Ginzburg-Landau Theory

The Ginzburg Landau (GL) theory is able to explan the *macroscopic* behavior of a superconductor. It is based on Landau's theory of thermodynamic transitions, according to which it is possible to treat phase transitions through an order parameter: null in the disordered phase and differs from zero in the ordered phase [13] [14].

GL introduces an order parameter, Ψ, a macroscopic wave function, capable of describing the entire superconducting system, written as:

$$\Psi = \sqrt{n_s(\mathbf{r})}e^{i\theta(\mathbf{r})} \tag{1.7}$$

where $n_s(r)$ is the density of the Cooper pairs, $\theta(r)$ is the phase [6].

The thermodynamic properties of the superconducting state can be described in terms of free energy F(T)=U-TS, where U, T ans S represent the internal energy, the temperature and the entropy respectively. Near the critical temperature, it can be expanded in terms of $\Psi(r)$:

$$F_S(T) = F_N(T) + \int \left(\frac{1}{2m^*}|(-i\hbar\vec{\nabla} - 2e\vec{A})\Psi(\vec{r})|^2 + a(t)|\Psi|^2 + \frac{1}{2}b(T)|\Psi|^4\right)d^3r \tag{1.8}$$

where $F_N(T)$ is the free energy of the normal state, $\alpha(T)$ and $\beta(T)$ are two phenomenological parameters, and F_S(T) is a functional of the order parameter Ψ. $F_S[\Psi]$is called *Landau functional* [14].

To determine the minimum of free energy, we can use the *variational method* minimizing the free energy $F_{\mathrm{S}}(T)$ with respect to Ψ^*(o Ψ) and to the vector potential $\vec{A}$ to obtain the *first equation of Ginzburg-Landau*:

$$a\Psi + b\Psi|\Psi|^2 - \frac{1}{2m^*}\Big(- i\hbar\vec{\nabla} - 2e\vec{A}\Big)^2\Psi = 0 \tag{1.9}$$

and the *second Ginzburg-Landau equation*:

$$\vec{J} = \frac{e}{m}\Big\{\Psi^*(-i\hbar\vec{\nabla} - 2e\vec{A})\Psi + cc\Big\} \tag{1.10}$$

last equation is able to describe the current flowing inside a superconductor.

Where 1.9 and 1.10 connect the two phenomenological quantities previously introduced, $a(T)$ and $b(T)$, to empirically known quantities: the critical field $H_c(T)$ and the effective penetration length magnetic $\lambda_{eff}(T)$.

By using the first Ginzburg-Landau equation, we can obtain information on the *coherence length* $\xi_{GL}(T)$:

$$\xi_{GL} = \sqrt{\frac{\hbar^2}{2m^*|\alpha(T)|}} \tag{1.11}$$

and, assuming the approximation $\alpha(T_c) \sim \alpha_0(T - T_c)$ and $\beta(T_c) \sim \beta_0$ (α_0 and β_0 defined positive), such that $\alpha(T)$ vanish for T_c and results negative below T_c, we obtain its temperature dependence gives by

$$\xi_{GL} = \frac{\hbar^2}{2m^*|\alpha_0|}\begin{cases}(\frac{T}{T_c} - 1)^{-\frac{1}{2}} \text{ for } T > T_c \\ (1 - \frac{T}{T_c})^{-\frac{1}{2}} \text{ for } T < T_c\end{cases} \tag{1.12}$$

The correlation length depends on the type of conductive material and on the temperature. Typical values of ξ_{GL} are shown in table 1.3.

Metal	ξ_{GL} **(nm)**
Al	1600
Sn	230
Pb	83
Cd	760
NbN	~ 5
Nb	38
YBCO	1-3; ~ 0.24

Table 1.3: Coherence length values for both low and high critical temperature superconductors [10].

1.2.3 BCS Theory

In 1957 Bardeen, Cooper, and Schrieffer (BCS) formulated a theory with the aim of explaining the *microscopic* origin of the superconductivity. The BCS theory

originates from Cooper's idea: he considers that the charge carriers for the electric supercurrents consist of a system of two electrons, the so-called *Cooper pair* [7]. The mechanism that leads to have Cooper pairs is due to an electron-electron interaction mediated by a phonon (see figure 1.7): an electron interacts with the lattice by polarizing the ions in the vicinity and, a subsequent electron, interacts with the polarized positive ion. This interaction induces an overall attractive force between the two electrons that leads them to form a boson [15]. The electrons that

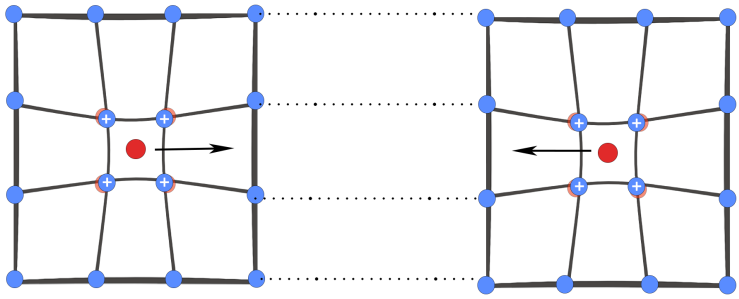

Figure 1.7: Schematic representation of the attractive interaction between two electrons (red filled circle) mediated by the lattice (blue circles) in order to create a Cooper pair.

form a Cooper pair have to have opposite spin and $\vec{k}$ vector: the total angular spin momentum of the pair is zero. Since the Cooper pair is a boson obeys the Bose-Einstein statistic. The interaction between two electrons is effective within a certain distance ξ, callled *coherence length*, which indicates the average distance at which the electrons are correlated to form a Cooper pair[7]. For temperature below T_c, all of these pairs form a strong correlated state, described by the same macroscopic wave function ψ.

The BCS Theory allows to interpret several experimental results. It predicts the existence of a band gap, $\Delta(T)$, with a temperature dependence shows in eq. 1.23.

$$\frac{2\Delta}{e} = \frac{2\Delta_0}{e} \tanh \sqrt{1 - \frac{T}{T_c}} \tag{1.13}$$

More details on BCS theory are provided in the appendix A.1.

1.3 Josephson effect

A Josephson junction is a system consisting of two weakly coupled superconductors (S), in which if the barrier is a thin layer of insulator the junction will be sketched as a S-I-S (Superconductor-Insulator-Superconductor), otherwise if it is a metal (Superconductor-Normal metal-Superconductor, SNS) or if the barrier is made by whatever material the system, with some constraints that will be soon explained, could represent a a Josephson junction [16].

When superconductors are very far apart, are described by their own wave function,

where their phases can be fixed arbitrarily, independently of others. Instead, if the superconductors are placed at a distance of about 10 Å, the Cooper pairs can flow from one superconductor to another, giving rise to a *non-dissipative* supercurrent[7], and keeping information on the phase difference between the two superconductors [16].

1.3.1 Josephson equations

Josephson junctions can be characterized by relationships that link the phase difference to macroscopic quantities. In the appendix A.2 is reported the procedure that allows to obtain the two Josephson equations:

$$I_s(\phi) = I_c \sin(\phi) \tag{1.14}$$

$$\frac{d\phi}{dt} = \frac{2eV}{\hbar} \tag{1.15}$$

where I_c indicates the critical current through the junction, and ϕ represents the phase difference between the two superconductors.

The former equation shows the dependence of the supercurrent on the phase difference between the two superconductors in absence of an applied potential (called DC Josephson effect), while equation 1.14 emphasizes how the phase difference changes over time when a potential difference appears between the two superconductors (called AC Josephson effect): assuming V = 0, it results that the difference phase is constant, but not necessarily zero. Therefore a finite current can flow through the barrier despite the absence of difference potential at the ends of the junction [17].

1.3.2 RCSJ model

Josephson junction can be modeled by using the Resistivity - Capacitively - Shunted - Junction (RCSJ), represented in figure 1.8. Solving the electronic circuit in fig.

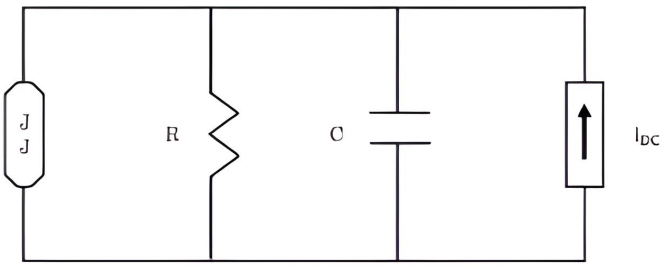

Figure 1.8: Resistively and capacitively shunted model of a Josephson junction (RCSJ) [18].

1.16, assuming the ideal junction, in parallel with resistance and capacity, the following relation is obtained:

$$I = C\frac{dV}{dt} + \frac{V}{R} + I_C sin(\phi) \tag{1.16}$$

then, using eq.1.14 and 1.15:

$$I = \frac{\phi_0 C}{2\pi}\frac{d^2\phi}{dt^2} + \frac{\phi_0}{2\pi R}\frac{d\phi}{dt} + I_c \sin\phi \tag{1.17}$$

we obtain:

$$I - I_c \sin\phi = -\frac{2\pi}{\phi_0}\frac{\partial U_j}{\partial \phi} \tag{1.18}$$

equivalent to the equation of motion of a phase particle moving in the *washboard potential*, U_j in eq. 1.19:

$$U(\phi) = \frac{\phi_0}{2\pi}\left[I_c(1 - \cos\phi) - I\right] \tag{1.19}$$

subject to a viscous force. It is observed that as the value of the injected current increases, the slope of the potential, and the probability that the phase particle escapes from the well, thus producing a phase slip and 'slips' increases [7].

- For $I < I_c$ the particle oscillates locally in the wall, the phase does not change over time and the junction is in the zero voltage state;

- for $I > I_c$ the minimum of the potential becomes a flex, and the particle moves easily along the potential; the time derivative of the phase, different than zero, generates a voltage across the junction and the system passes to the resistive state.

RCSJ model provides further parameters like the quality factor of the junction, Q, which also depends on the capacity of the junction according to equation 1.20:

$$Q = \sqrt{2eI_c\frac{CR^2}{\hbar}} = \omega_{\mathrm{p}} RC \tag{1.20}$$

with ω_{p} the *plasma frequency*. It is important to note that the I-V characteristics of a Josephson junction are strongly influenced by the capacity of the junction because it determines, as reported in figure 1.9, its trend [1].

If Q<1 the junctions regime is called *overdamped*: C assumes small values (< fF), the equation can be analytically solved, and a non-hysteretic IV characteristic is obtained (see figure 1.9 (a)). Junctions with metallic or ferromagnetic barriers are typically in the overdamped regime. In other words, the barrier is not insulating;

If Q>>1 the system is in the *underdamped regime*, then the capacity is large, and the IV shows a hysteretic curve 1.9 (b). Usually, in this case, the junctions include an insulating barrier.

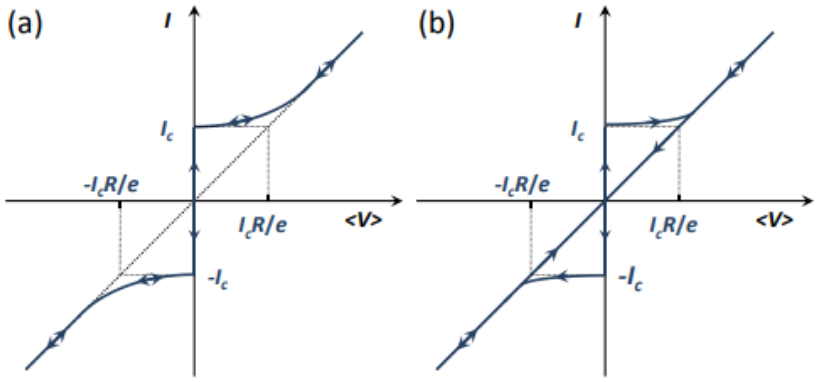

Figure 1.9: Current-Voltage curve of an a) overdamped and b) underdamped (b) Josephson junction. Image adapted from [19].

1.4 SIS junction

In this section, we will focus on two superconductors spaced by a thin insulating layer to form a Superconductor-Insulator-Superconductor (SIS) structure.

1.4.1 Temperature dependence

The Josephson junction parameters strongly depend on the temperature. Various theories have been developed for the specific junction layouts and configurations useful investigate their temperature dependence of I-V curves. For SIS JJ, Ambegaokar and Baratoff using Green's function approach found the following relation 1.21 [6]:

$$\frac{eI_S(\phi)R_N}{2\pi T_C} = \frac{T}{T_c}\sum_{\epsilon>0}\frac{\Delta_L\Delta_R}{\sqrt{(\omega^2+\Delta_L^2)(\omega^2+\Delta_R^2)}}sin(\phi). \tag{1.21}$$

where I_s is the superconducting current, R_N is the normal resistance, T_c is the critical temperature, $\Delta_{L,R}$ is the potential gap of the superconductor, and ω are the Matsubara frequencies [6].

Starting from 1.21 an approximated but experimentally useful formula leads to the eq. 1.22:

$$I_cR_n = \frac{\pi\Delta}{2e}tanh\left(\frac{\Delta}{2kT}\right) \tag{1.22}$$

where an increase in temperature determines a suppression of the critical current I_c.

For T=0 the eq. 1.22 assumes the over simplified form reported in 1.23.

$$I_cR_n = \frac{\pi\Delta(0)}{2e} \tag{1.23}$$

1.4.2 Magnetic field dependence

Generally, the action of an external magnetic field perturbs the properties of the junction giving rise to space modulation of the phase [20].
The $I_c(H)$ strongly depends on the shape and morphology of the junction. Most

junctions have rectangular cross sections, while those investigated in this work are circular thus generating specific fingerprints in the $I_c(H)$ shape that will be explained in the next chapters.

Rectangular Josephson junction

Consider a magnetic field in the $\hat{y}$-direction of the junction represented in figure 1.10. Applying the theory of GL it is possible to derive:

$$\Delta\phi = \frac{2e}{\hbar c}\left(\frac{mc}{2e^2\rho}\vec{J}_s + \vec{A}\right) \tag{1.24}$$

where $\vec{A}$ is the potential vector linked to the magnetic field, ρ is the density of Cooper pairs, m is the mass of the electron and $\vec{J}_s$ is the current density. Assuming that the thickness of the superconducting films is greater than the London penetration length, and assuming negligible the thickness of the barrier with respect to the size of the junction, is obtained:

$$\frac{d\phi}{dx} = \frac{2e}{\hbar c}(\lambda_L + \lambda_R + t)H_y = \frac{2e}{\hbar c}dH_y \tag{1.25}$$

where λ_L and λ_R are the London penetration lengths of the superconductors and t is the thickness of the dielectric barrier, while their sum d is called magnetic penetration. Integrating equation 1.25, the supercurrent can be expressed as:

$$I(x, H_y) = I_c sin\left(\frac{e^*}{\hbar c}dH_y x + \phi(0)\right) \tag{1.26}$$

In short junction limit (L << λ), the magnetic space d is:

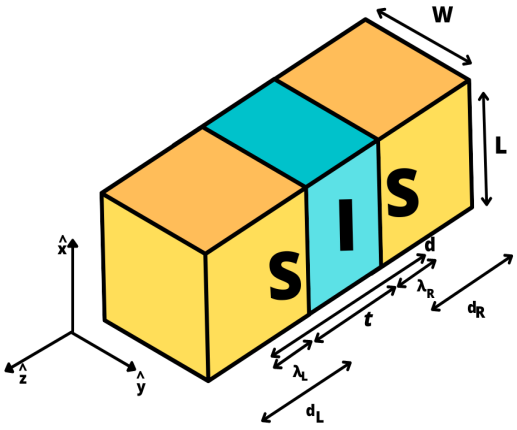

Figure 1.10: Sketch of a SIS Josephson junction. $d_{L/R}$ and t represent the thickness of S, and I layer respectively while W is the width and L the length of the junction.

$$d = t + \lambda_L coth\left(\frac{d_L}{\lambda_L}\right) + \lambda_R coth\left(\frac{d_R}{\lambda_R}\right) \tag{1.27}$$

where d_L (d_R) are the electrode thicknesses. Substituting this relation within 1.14, yields the relation 1.28..

$$I_c(H) = I_{cmax}\left|\frac{sin\left(\pi\frac{\phi}{\phi_0}\right)}{\left(\pi\frac{\phi}{\phi_0}\right)}\right| \tag{1.28}$$

with $\phi = H_y L t$ the magnetic flux through the junction and $\phi_0 = \dfrac{h}{2e}$ the quantum flux.

Equation 1.28 looks like that for the optical Fraunhofer diffraction pattern.
The minima occur at values of the magnetic flux within the barrier equal to multiples of the flux quantum[1] [6]. The periodicity of the pattern is given by

$$\Delta H = \frac{\phi_0}{Ld} = \frac{\phi_0}{L(\lambda_L + \lambda_R + t)} \tag{1.29}$$

and if the two superconductors are equal ($\lambda_L = \lambda_R$) we obtain an experimental method for the determination their London penetration depth.
When the thickness of the superconducting films are small compared with λ_L the periodicity of $I_c(H)$ plot is reported in eq.1.30.

$$\Delta H = \frac{\phi_0}{L\Big(\lambda_L \tanh \frac{d_L}{2\lambda_L} + \lambda_R \tanh \frac{d_R}{2\lambda_R} + t\Big)} \tag{1.30}$$

where d_L and d_R are the thicknesses of the superconducting electrodes [1].

Circular Josephson junction

When the JJ assumes a circular shape the $I_c(H)$ relation changes having the form reported in eq.1.31 (called Airy pattern).

$$I_1(k) = I_1 \left| \frac{J_1(kR)}{\frac{1}{2}(kR)} \right| \tag{1.31}$$

where $I_1 = \pi R^2 J_1$, $J_1(x)$ is a Bessel function of the first kind, $k = \frac{2\pi d}{\phi_0}$, and R is the radius of the junction [1][6]. The periodicity of $I_c(H)$ is defined as half the amplitude of the first lobe of the Fraunhofer pattern is given by:

$$\Delta H = \frac{\phi_0}{Rt} \tag{1.32}$$

1.5 SNS junction

When two superconducting banks are coupled through a normal barrier the overall superconductor-normal-superconductor (SNS) Josephson junction is passed by a superconducting current that could be predicted by using models that differ from from those of a SIS junction [16] [21].

1.5.1 Proximity effect at S/N interface

When a superconductor is placed in close contact with a normal metal proximity effect occurs [22]: Cooper pairs penetrate inside the normal metal (N) and N acquires part of the superconducting properties near the interface [23]. Ginzburg Landau's theory can give direct insights into the occurrence of the proximity effect and on the scaling lengths. The macroscopic wave function, in equation 1.33, capable of

describing the entire system in the N region exponentially depending on the distance from the S/N interface.

$$\psi = \psi_0 \exp\left(-\frac{x}{\xi_N}\right) \tag{1.33}$$

where ξ_N is the coherence length of the Cooper pairs within the metal (see figure 1.11). The proximity effect can be expressed through the microscopic process of

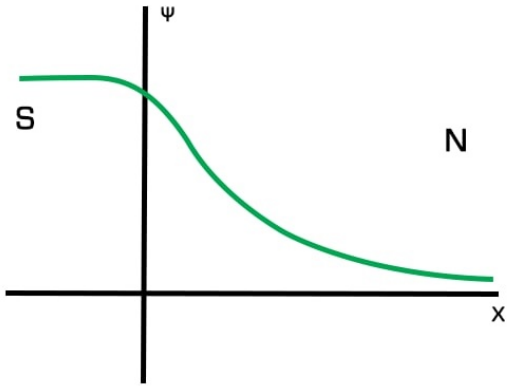

Figure 1.11: Behavior of superconducting order parameter in a S/N interface.

Andreev reflection, which is treated in appendix A.3.

1.6 SFS junction

The sketch of a SFS junction is given in figure 1.12. In order to discuss the trans-

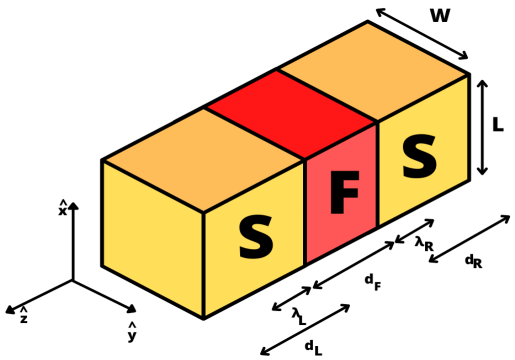

Figure 1.12: Sketch of a Josephson junction in which the barrier is made of a ferromagnetic material. Sketch of a SFS Josephson junction. $d_{L/R}$ and d_F represent the thickness of S and F layer respectively while W is the width and L the length of the junction.

port properties of a Josephson junction characterized by a barrier of ferromagnetic material it is necessary to understand how it behaves when interacts with a superconducting material [5] [24].

1.6.1 Ferromagnetic properties

Ferromagnets represent a class of materials that below a temperature, called Curie temperature, if immersed in a magnetic field, remain magnetized even when the field

cancels out. The magnetization originates from the *exchange interaction* between the magnetic dipoles that opposes thermal agitation [19]. In fact, as shown in the figure 1.13, as the temperature increases, spontaneous magnetization decreases, and above the Curie temperature a ferromagnetic material behaves just like a paramagnet [18][19].

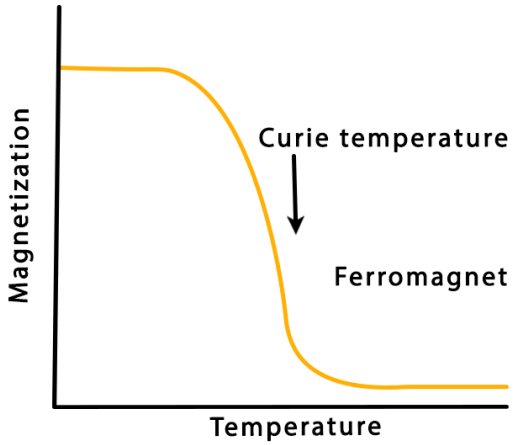

Figure 1.13: Schematic illustration of Magnetization vs Temperature curve for Ferromagnetic materials.

The magnetization is given by:

$$\vec{M} = \frac{1}{\mu_0}\vec{B} - \vec{H} \tag{1.34}$$

and it can be expressed as:

$$M(T) = \frac{N}{V}\mu_B tanh\Big(\frac{1}{k_b}\frac{MV}{N\mu_b}\frac{Z}{2}J\Big) \tag{1.35}$$

where N is the total spin number, V is the ferromagnet volume, Z is the coordination number, μ_B is the Bohr magneton and J is the coupling constant equal for all spin pairs [18][19][25] .

Ferromagnet materials are composed of many domains, and since direction of the magnetization of each domain is random, the overall magnetization is zero.
When an external magnetic field is applied, the ferromagnet shows an hysteretic behavior such as that sketched in figure 1.14. The first time the field is applied to the ferromagnet, M increases linearly with H, until saturation is reached H_s (orange curve in figure 1.14). Then, a decreasing external magnetic field is applied to the ferromagnet and domains start to change their magnetization, until the value $-M_s$ is reached. At this point, by applying an increasing external magnetic field, the ferromagnet changes its magnetization following a new curve.

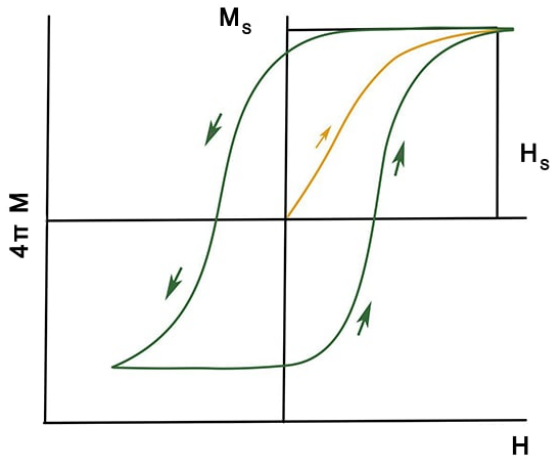

Figure 1.14: Magnetization as a function of the applied magnetic field curve for a ferromagnet material.

1.6.2 Proximity effect at S/F interface

In the case of an S/F interface, two competitive phenomena take place: the presence of Cooper pairs, characterized by electrons with opposite spin and the presence of ferromagnetic materials, in which an external field promotes the alignment of spins along the same direction. The exchange field also determines the coherence length in the ferromagnetic material and is such that the Cooper pairs acquire a finite momentum, promoting an oscillation of the order parameter [19] [22].
The spatial modulation of the order parameter is due to the *Zeeman splitting* [22] [19] of the electronic levels in the presence of the exchange field: the spin-up electron of the Cooper pair, with direction parallel to that of the external field, reduces its potential energy and increases the kinetic energy by a quantity h=$\mu_B H$, while the electron with spin down increases its potential energy. The Cooper pairs acquire a moment $2\delta k = \frac{\mu_B H_{ex}}{v_F}$. [22].

The proximity effect in the case of an interface of the S/F type can be treated by using the Ginzburg Landau theory [22] [26].

$$\Psi = \Psi_0 e^{kx} \tag{1.36}$$

where k is a *complex wave-vector*, written as $k = k_1 + ik_2$. The order parameter for the system in question takes the form of 1.36 and looks like in figure 1.15.
More details are contained in[22].

This non-uniform superconducting state was predicted by Fulde, Ferrel, Larkin and Ovchinnikov, FFLO state, in 1964 [22].

In the case of an SFS junction, the critical current is subject to oscillations as the thickness of the barrier varies, due to the damped oscillatory behavior of the superconducting order parameter and the presence of an FFLO state [22]. The correlation decay length in the ferromagnet is:

$$\xi_F = \sqrt{\frac{\hbar D_F}{2\pi h}} \tag{1.37}$$

where h is the exchange energy and D_F is the diffusion coefficient of the ferromagnet.

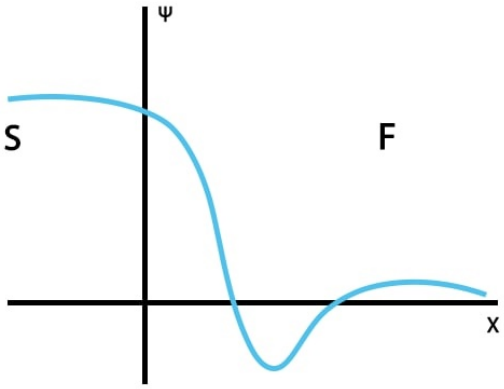

Figure 1.15: Behavior of superconducting order parameter in a S/F interface.

When the incident wave at the S/F interface will interfere with the wave reflected from the opposite surface of the F layer, there will be different behaviors as the thickness of the ferromagnetic layer varies:

- for F layer thickness smaller than ξ_F, the pair wave function in the F layer changes a little and the superconducting order parameter in the adjacent S layers is the same; we have a "0"-phase state;
- if F layer thickness becomes of the order of ξ_F, the pair wave function may go through zero at the center of F layer, providing the state with the opposite sign, in the way to obtain a "π"-phases state.

Generally, in ferromagnetic junctions the order parameter allows us to observe numerous phenomena, such as *0*-π transitions, dependent on the thickness of F [22].

An interesting case of π junction is given by a Superconductor/ Insulator /Ferromagnet /Superconductor (SIFS) Josephson junction, a S/F/S trilayers with one transparent interface and a tunnel barrier between S and F layers [22].

1.6.3 SFS junction in magnetic field

If a magnetic field is applied to a rectangular junction, its dependence of I_c as a function of H is represented by the Fraunhofer pattern (sec. 1.4.2) [3][27] [28]. In the case of a SFS junction, we obtain a shifted Fraunhofer Pattern, and this phenomenon is due to the fact that for SFS junctions we have even to take into account the flux due to the magnetization of the ferromagnetic layer below the Curie temperature [29].

The flux due to the magnetization of the ferromagnetic barrier is

$$\phi_F = \mu_0 M d_F L, \tag{1.38}$$

where d_F is the thickness of the ferromagnetic layer (1.12) and M is the junction magnetization [30]. The total flux will be given by eq. 1.39.

$$\phi = \phi_F + \mu_0 H L d_M. \tag{1.39}$$

thus causing the shift of the pattern. Replacing the 1.39 in 1.28, we obtain:

$$I_C(H) = I_C(0)\left|\frac{\sin\left(\pi\frac{\phi_F(H)\pm\phi_M(H)}{\phi_0}\right)}{\left(\pi\frac{\phi_F(H)\pm\phi_M(H)}{\phi_0}\right)}\right| \tag{1.40}$$

that means that the hysteretic behavior of M(H) in ferromagnets gives rise to a hysteretic behavior of I_c, shown in 1.16. In figure 1.16-a is displayed how by mag-

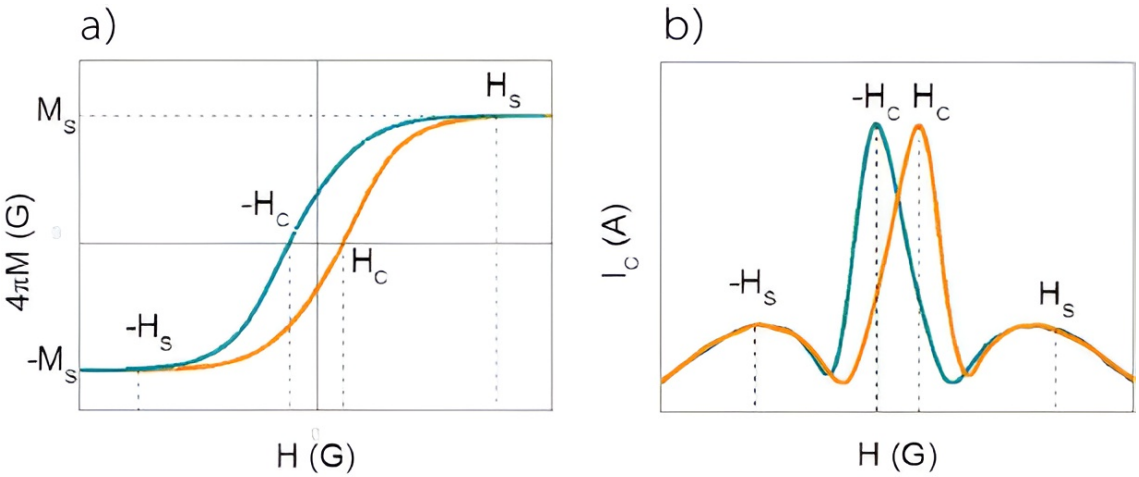

Figure 1.16: It shows a)hysteretic curve for a ferromagnet; b)behavior of the critical current versus external magnetic flux [20].

netizing the ferromagnet two nonsuperimposable Fraunhofer patterns are observed, reducing the magnetic field from positive to negative values; the maximum of the critical current is shifted towards negative values of the magnetic field (green line in 1.16-b), while as the magnetic field is swept from negative values to positive (orange line in 1.16-b), the maximum of the critical current is shifted towards positive direction of the magnetic field [30]. Because of these properties, SFS JJs are suitable as RAM (Random Access Memories) memories [5].

1.7 SIs'FS junction

Generally, SFS JJ's are known as dissipative elements, due to the presence of the ferromagnet [31] [32][33]. In order to reduce its dissipation, an insulating layer is added to the junction to form a layout (SIs'FS) such as that shown in fig.1.17: where S is a bulk superconductor, I is an insulator, s' is a thin superconducting film, and F is a metallic ferromagnet [29]. The geometry and size of the devices have an obvious influence on properties of the junction. As an example, in figure 1.18, the value of the I_cR_n parameter for different values of the F-layer thickness, and for different reference JJs are reported [33]. We can observe that:

- for the black, blue and orange curves the thickness of the middle s' layer is much larger than that of s layer, $d_{s'} >> d_{S_c} = 3\xi_S$ [34]. In this case the structure can be considered as a serie of SIs' and s'FS junctions. The properties of the structure are determined by the junction that shows the smallest critical current amplitude. In the ordinary case of $I_{c_{SIs'}} << I_{c_{s'FS}}$, the junction behaves like a conventional SIS with an important distinction:

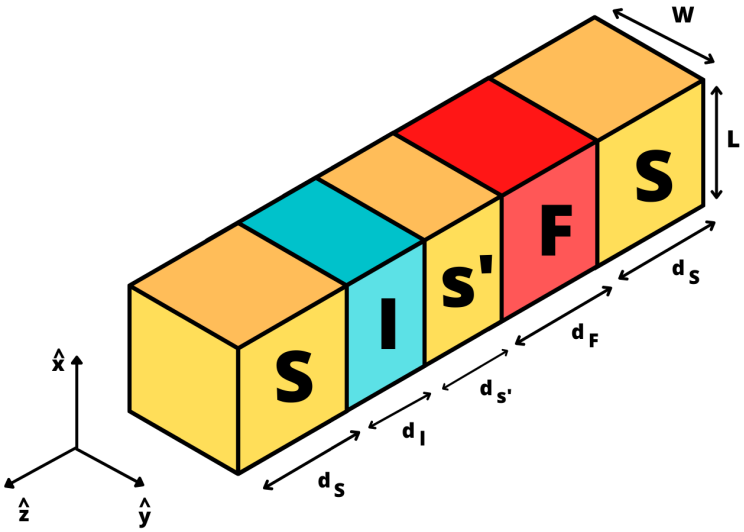

Figure 1.17: Sketch of a SIs'FS Josephson junction. d_S, $d_{s'}$, d_I, d_F, represent, the thickness of S, s',I and F layer respectively while W is the width and L the length of the junction.

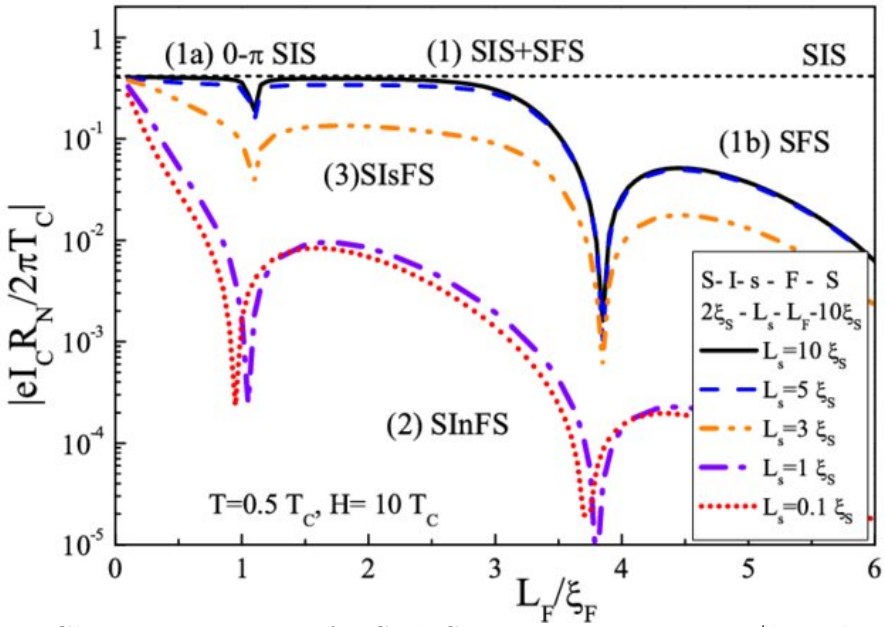

Figure 1.18: Characteristic I_cR_n for SIs'FS structures versus L_F/ξ_F; where L_F and ξ_F represent the thickness of the F-layer and its coherent length, respectively. The image has been adapted by [33].

the s'FS junction can turn the SIs'FS structure into a π-state [34]. Therefore, the structure can be called switchable 0-π SIS junction [34].
Another case appears for *large* d_F values and high exchange fields H. Namely, the structure transforms into a standard SFS-junction without any influence of tunnel barrier [34].

- the purple dashed curve describes the case of juntions with $d_{s'} < d_{S_c}$: it leads to the suppression of superconductivity completely appears, and drives the

formation of a complex-InF-weak link area. In this case the critical current I_c is close to that shown by SIFS junctions. The system behaves such as a single SInFs junction [34].

- The intermediate case occurs when $d_{s'} \sim d_{S_c}$. The system is sensitive to the F-layer parameters (thickness d_F and exchange field H) that control the suppression of superconductivity in the s'F bilayer.

1.7.1 SIs'FS junction in magnetic field

In samples containing an F-barrier, to evaluate the total magnetic flux through the junction ϕ, we have to take into account the F magnetization flux ϕ_M, which is given by $\phi_M = \mu_0 M_F L d_F$, with L the cross-section width. Hence, the total magnetic flux through the junction is $\phi = \mu_0 H L d_M + \mu_0 M_F L d_F$, where the thickness of the material penetrated by the applied field is $d_M = 2\lambda_S + d_{s'} + d_F + d_I$, with $d_{s'}$ the thicknesses of the thin superconductor and d_I the thickness of the insulator [23] [30].

In this case, because the hysteretic dependence of M_F on H, it should observe a hysteresis of the $I_c(H)$ curve depending on the sweeping direction of H. The resulting Fraunhofer patterns are shifted in the field to a point where the flux due to the external field cancels out the flux due to the magnetization. Specifically, we expect that, when H is ramped from positive to negative fields (black curve in 1.19 a), the global maximum of the Fraunhofer-like pattern should be shifted toward negative (black curve in 1.19 b) fields because of the positive remanence of the F layer, whereas when H is ramped from negative to positive fields (red curve in 1.19 a), it should be shifted toward positive fields (red curve in 1.19 b)[30]. In the simple

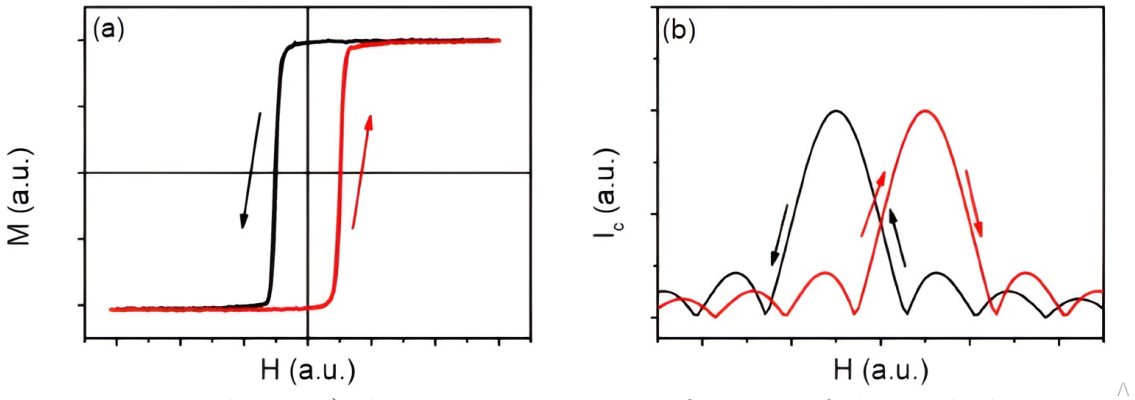

Figure 1.19: It shows -a) the magnetization as a function of the applied magnetic field for a superconducting junction employing a ferromagnetic layer; b) the magnetic dependence of the critical current; the black solid curve is made by positive magnetic field (H) while the red by negative H [30].

case of a homogeneous F barrier in a single domain state, the Fraunhofer pattern is simply offset by a factor

$$\mu_0 H_{shift} = -\frac{\mu M_F d_F}{(2\lambda_S + d_{s'} + d_F + d_{ox})} \tag{1.41}$$

where M_F is the saturation magnetization of the F layer.

Inverse proximity effect

The inverse proximity effect occurs when the magnetic moment m is transferred from the F to the S system. This phenomenon is related to the Cooper pairs localized in proximity to the S/F interface: an electron with the spin aligned along the exchange field can easily penetrate the F layer, while an electron with the opposite spin tends to stay in the S layer. As result, the superconducting coherence length ξ_s ($\sim$ 1-100 nm) acquires a net magnetization M_{Sc} with opposite direction to M_F. Neglecting this short-range inverse proximity effect and the stray fields of the F layer, the direct S/F proximity effect is always responsible for the generation of screening supercurrents in response to the presence of a vector potential at the S/F interface, the so-called electromagnetic proximity effect. These supercurrents generate a magnetic induction field B_{Sc} in the S film which is antiparallel to M_F and decays at distances of the order of the London penetration depth λ_S. The profile of the magnetic induction in S at the S/F interface is

$$B_{Sc} = -\mu_0 M_F Q exp\Big(\frac{x}{\lambda_S}\Big) \tag{1.42}$$

with $Q = \int_0^{d_F} \frac{x'}{\lambda_S^2} dx$ where x is the axis orthogonal to the S/F interface where the origin has been set [23][30].

According to the inverse proximity theory, the magnetization in the S at the interface with F, M_{Sc} cannot exceed the value of M_F. Therefore, if we suppose that, in the SIs'FS JJs, we are in the presence of a magnetization M_{Sc} induced by the inverse proximity effect in two S layers adjacent to the F, and we assume that two S/F interfaces are identical, neglecting the electromagnetic proximity effect and the stray field, the total magnetic flux through the junction is:

$$\phi = \mu_0 H d_M L + \mu_0 M_F(H) d_F L(1-\gamma) \tag{1.43}$$

where γ is a parameter that considers the contribution to the total flux through the junction caused by the spin polarization in the S:

$$\gamma = \left| \frac{M_{Sc}}{M_F} \frac{2\xi_s}{d_F} \right| \tag{1.44}$$

To observe the inverse magnetic hysteresis γ must be larger than unity [30]. The choice of the materials and the geometry of the device, along with the characteristic lenght scales of the S and F layers, and in particularly the ratio $\frac{\xi_s}{d_F}$ play a crucial role in the observation of the inverse magnetic hysteresis.

Chapter 2

Introduction to the fabrication process

This chapter will focus on the fabrication processes useful to build the Josephson junctions, investigated in this thesis. Therefore I will introduce the photolithography and I will describe the used deposition techniques.

2.1 Protocol of fabrication

In this section, I will report on the realization and characterization of SIs'FS JJs multilayer devices, based on an Nb technology, that has been studied in this thesis work [5] [35] [36].

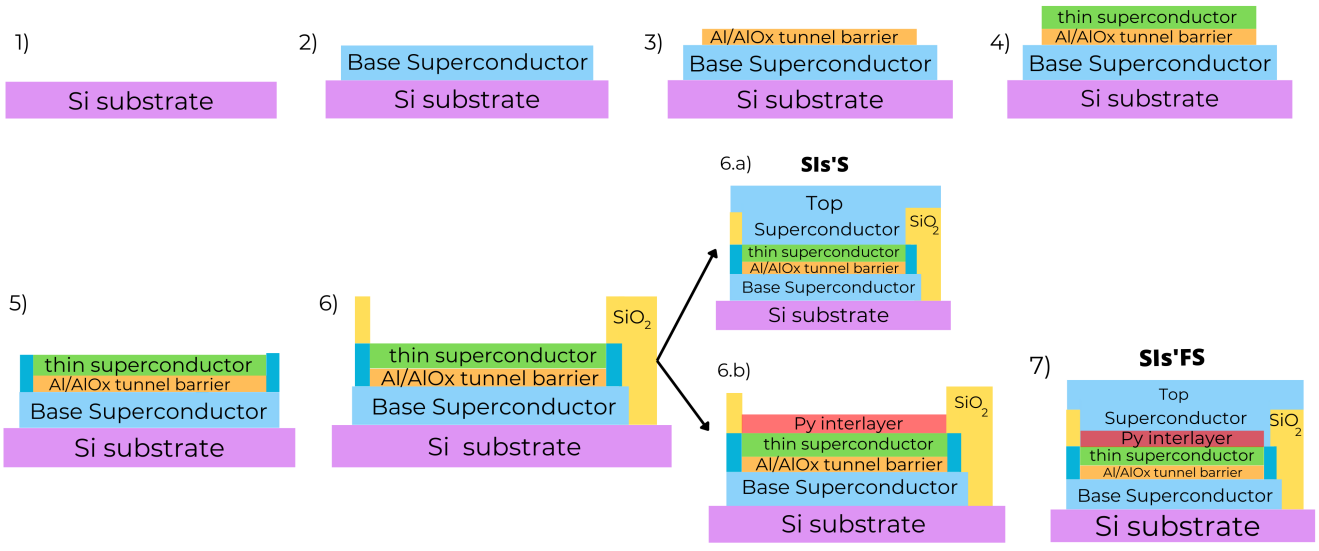

Figure 2.1: Schematic representation of the developed fabrication processes useful to build the investigated Josephson junctions.

Figure 2.1 shows all the processes inherent to the fabrication:

- 1) Si wafer is cleaned by Aceton and Isopropanol;

- 2)-3) a thin superconducting layer (Nb or Al) is deposited followed by Al deposition that, when oxide, forms the insulating barrier;
- in 4) a Nb-Al/AlOx-Nb trilayer has been deposited in an ultra-high vacuum system by dc magnetron sputtering onto oxidized Si wafers. The base electrode consist of Nb film having a thickness of 200 nm, while the top electrode consists of Nb film having a thickness of 40 nm. Both electrodes are deposited at a rate of 1.2nm/s. The intermediate Al layer has been deposited at a small rate of 0.7nm/s to obtain a film thickness of 7nm, which afterward is exposed to dry oxygen to form AlOx tunnel barrier. The trilayer has been patterned using optical lithography and lift-off procedure;
- in 5)-6), we used a selective anodization process, togeher with further insulation by SiO_2 deposition, to obtain the junction areas. The dimension of the area of the JJs ranges from 100 μm^2 to 7 μm^2;
- 6.b), the wafer has been diced into 10×10 mm^2 chips, and Ar ion etching has been used to remove 10 nm of the Nb oxide layer before depositing the F layer. A layer of Py has been deposited by the lift-off technique. The Py has been sputtered by a magnetron source at a rate of 0.7 nm/s;
- Py films have been analyzed using a scanning electron microscope (SEM), equipped with a probe for energy dispersion spectroscopy (EDS probe), to obtain a chemical analysis of the surface;
- then, 7) a 400nm top Nb counter electrode has been deposited by dc-sputtering and lift-off process, obtaining the overall SIs'FS structure.

The optical image reported in figure 2.2 shows the chip layout of the studied junctions.

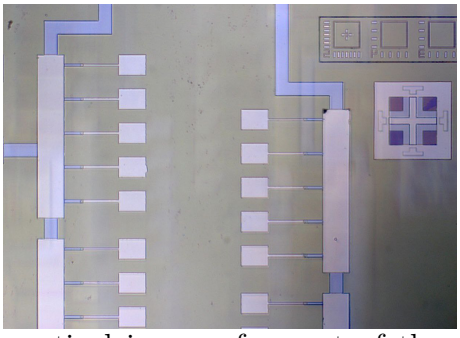

Figure 2.2: It shows the optical image of a part of the develop chip layout that includes the superconducting junctions investigated in this thesis work.

The investigated junctions are:

- SIs'S Josephson junctions, based on Niobium;
- SIs'FS Josephson junction, based on Niobium, for $d_{s'}$=30 nm, and $d_{s'}$=10nm;
- SIs'S and SIs'FS Josephson junction, based on Aluminium [35].

The realization of these other junctions took place following the same procedures described above. In particular, in the case of the SIs'S junctions, the steps for the deposition of the ferromagnet were not performed, following points 1 to 6 sketched in figure 2.1. For junctions having different thicknesses of s' layer, the parameters of the instruments were set differently, while junctions based on Aluminum or Niobium, different superconductors have been used.
In this case, it should be emphasized that, while junctions based on a Niobium technology have been extensively studied in the literature, that made using Aluminum technology represent a novelty and it is the first time that they are investigated.

2.2 Photolithography technique

Lithography techniques allow to transfer a pattern onto a film by using a photosensitive polymer (resist). It is based on UV-source since it is faster (a few seconds of exposure for having a complete exposure of an entire 8" wafer, against several hours necessary if using an electron beam-based lithography) and less expensive. The substrate is first *cleaned* (2.1-2) to remove dust and contaminants from the surface. Then, is covered with UV resist (2.1-3), a polymer sensitive to UV light, by *spin-coating*: the sample is placed on rotating support (spinner), a few drops of the resist dispensed on it, then it is put into rotation in order to spread the fluid on the substrate. The parameters of rotation are calibrated to establish the needed thickness of the resist, allowing better evaporation of the solvent and the formation of a solid and uniform thin film. The thickness of the resist depends on the concentration of the polymer in solution and its viscosity and is reduced as the rotation speed increases. The *soft-bake* process occurs when heating is used at 80-90° C, to evaporate the residual solvent from the resist. During the *exposure step*, the sample is irradiated by a UV lamp and *aligned* to a mask in quartz. The UV light on the sample sensitizes the resist in correspondence with the openings of the mask. Exposure to light modifies the chemical bonds of the resist then a chemical solution, called "developer" allows to dissolves only the exposed resist (see sketch 2.1-4).

- For positive resist the developer dissolves the part of resist that has been exposed; positive resist allows to transfer in the resist the same pattern drawn on the mask;
- The negative resist allows to transfer the complementary drawn design on the mask.

2.3 Deposition techniques

The superconducting materials are deposited by DC magnetron sputtering. This technique allow to deposit thin film with high uniformity of thickness. The deposition step is run in an Ultra High Vacuum (UVH), about 10^{-7} Torr chamber [37]. The used deposition systems are located at the superconductivity laboratory of the Department of Physics and of the CNR-SPIN center-Pozzuoli, and at the Polytechnic School of the Basic Sciences of the University of Naples' Federico II.

2.3.1 Sputtering DC magnetron

DC sputtering process is sketched, in figure 2.3.
We can distinguish between :

- the *target* (blue rectangle), the material to be deposited, connected to a power supply DC. The target is bombarded by energetic particles, mainly ions, which cause the detachment of atoms or molecules that are deposited on substrates; the process takes place in an isolated environment.
- the *substrate* (green rectangle), the material on which to carry out the deposition, connected to the ground.

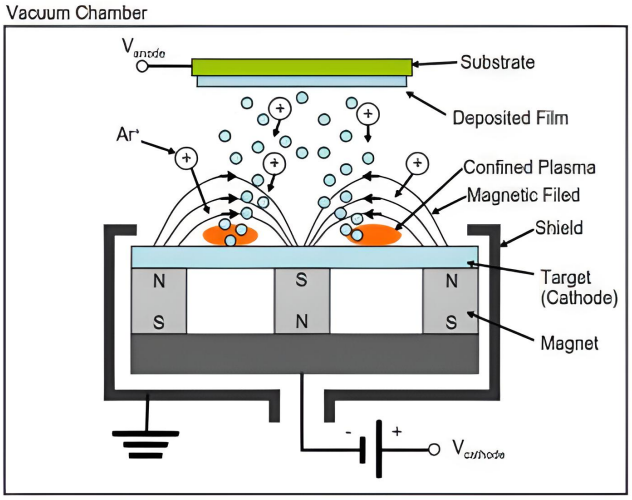

Figure 2.3: Sketch of a DC magnetron sputtering system.

Ions come from an inert gas at low pressure, noble gas, to avoid the compromising growth of the thin film, which is inserted inside the chamber between two electrodes [37].

By applying a difference of potential between the target and the ground, an electric discharge is obtained which ionizes the gas and gives the plasma (orange one in 2.3), consisting of positive Ar^+ ions and free electrons, accelerated by the electric field towards the target going to free. It is possible to observe phenomena of chain multiplication, due to secondary electrons going through a mechanism of ionization events. The number of electrons will not increase indefinitely since there will always be recombination favored by the chamber walls. At equilibrium, the number of electrons and ions produced is equal to those of the recombination process [37]. To increase the efficiency of the sputtering process it is possible to confine the discharge near the target using permanent magnets, favoring the confinement of secondary electrons near the target surface, and due to their spiral shaped path, increasing the probability of ionization due to gas collision. This, therefore, allows to decrease the pressure of the sputtering gas and consequently reduces the concentration of impurities in the environment. This variant of the process, called *magnetron sputtering* improves the potential of the technique, in particular by increasing the deposition and the efficiency of the deposition.

Chapter 3

Measurements, techniques and experimental set-up

The electronical characterization of superconducting materials requires a system that allows to reach low temperatures, equipped with cryogenic filters useful to remove unwanted sources of noise. The electrical characterization has been performed in Triton cryostat, to which I contributed to installing lines and setting up the electronic setup. Triton system is a cryogen-free system, suitable for long-term and less-expensive cool-downs.
The next sections are dedicated to the description of the main features of the Triton and its filtering system. In addition, I will give an overview of the techniques used to perform DC- measurements for Josephson junctions.

3.1 Triton Dilution fridge

Oxford Triton system reported in figure 3.1 is a helium-free cryostat that allows to reach temperature below 10mK.

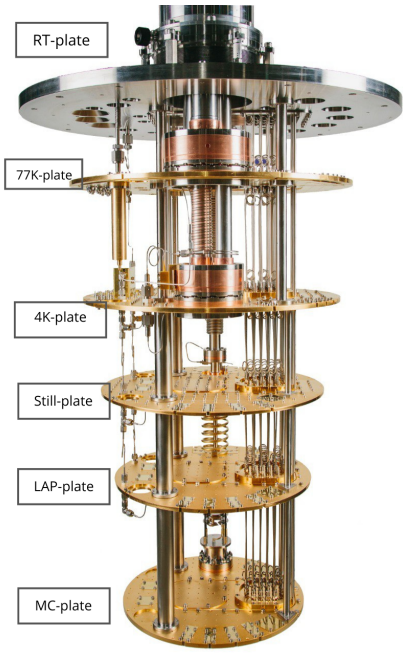

Figure 3.1: Lateral view of the Triton system.

It is equipped of six copper gold-and silver-covered plates, thermally decoupled one from another by means of Stainless-Steel (SS) supports [38]. The plates distribution is the following:

- the RT-plate, at RT;
- the PT1, at $\sim$ 70K;
- the PT2, at $\sim 4.2K$;
- the still-plate, at $\sim 700mK$;
- the IAP-plate, or cold-plate, at $\sim$ 100 mK;
- the MC-plate, at $\sim 10mK$.

The temperature of the last three plates is determined by the *dilution process*, proposed by Heinz London in 1950s, characterized by three main stages, which we will describe in more detail.

The first phase is the *condensation*, where an ^3He-^4He mixture gas, preserved in a tank, is first cooled and purified in liquid nitrogen. Then a pulse Tube Refrigerator (PTR) precools the system down to about 10 K. The PTR vibrations induce noise during the measurements, so, copper braids are used at the 4K-plate, capable to decouple the PTR heads from the other plates. In the Pre-Cooling (PC) phase the mixture is first cooled down to 10K using a series of heat-exchangers located at PT1, PT2, the still, the cold-plate and the Mixing Chamber (MC), and a counter-flow heat exchanger located at the top plate improves the cooling of the gas before it reaches PT1. When the system reaches $\sim 10K$, the pre-cool loop is evacuated using a turbo pump, and the mixture is compressed using a high pressure ($\sim$ 2.5 bar) pump. Then, the Dilution Unit (DU) starts and a series of heat exchangers and pressure impedance in the condenser line are used, in the way to reach temperatures below $\sim 2K$.
The ^3He, in the mixture, is still gaseous, so, combining the effect of an extra heat-exchanger in the still and an impendance in the JT stage, it reachs its condensing temperature. The circulation of the *mixture* through the condensing and still lines, by using the external pump rack, allows to reach a temperature of about 800 mK. For values below 800 mK, a phase boundary between the concentrated and the dilute phases of ^3He in the ^3He-^4He mixture occurs. The motion of the ^3He out of the MC is an endothermic process, called *dilution phase*, that lowers the temperature down to 10 mK. Finally, the ^3He molecules in the MC are pumped out through the still-line and then recondensed again (*circulation*). In the still chamber, which has optimal temperature between 700 mK and 800 mK, we can increase the evaporation of the mixture using a heater, and optimize the *circulation process*.

The control of the pumps, pressures, temperatures and valves in the cryostats is achieved with the use of an Intelligent Gas Handling system (IGH), driven by an Oxford Instruments LabVIEW software.

3.2 Measurement system

I will briefly describe the engineering, mounting and characterization of the DC-filtered electronics.

3.2.1 DC setup

Accurate measurement of the transport properties of JJs and superconducting nanostructures requires filters useful to reduce the electrical and thermal noise. The Triton is equipped with 48 DC-lines, 24 current-carrying lines and 24 voltage lines. Half of these lines (12 current lines and 12 voltage lines) are designed to be filtered.

From the RT-plate to the 4K-Plate, I-lines and V-lines are twisted pairs in copper and constantan DC-looms from Oxford instruments, respectively. From the 4K-Plate to the MC-plate, instead, I-lines are in a NbTi DC-loom from Oxford Instruments, while the V-lines are homemade manganin twisted cables The constantan and the manganin are characterized by a low thermal conductivity, and therefore suitable for voltage measurements. Copper lines are, instead, characterized by a lower resistance compared with the voltage-lines, thus reducing heating when current-biasing the devices. Finally, the NbTi is superconducting below 10K, i.e. it ensures no heat dissipation at the coldest stages of the cryostat.

The home-made wiring is electrically isolated from the environment with fiber glass gloves. Some sections of the wires are left uncovered for thermalization: the lines are spiraled around copper pillars thermally anchored at the 4K, the still- and the IAP-plates. Varnish glue ensures electrical insulation and favors thermalization.

RT to 4K

The first filtering stage is at RT via two EMI filters connected to the I and V input on the top of the cryostat. Such filters are composed of find ferrite beads followed by 24-channel filter boxes with paththrou RC-π filters (fig. 3.2).

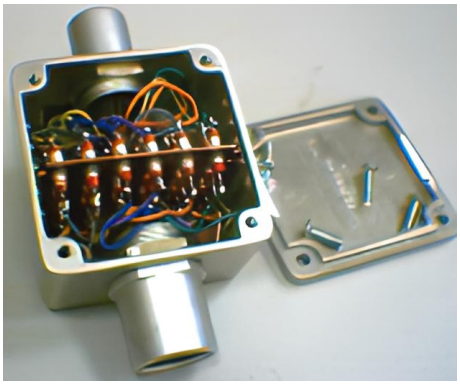

Figure 3.2: Emi filters used to improve the signal-to-ratio-noise. They are connected, at room temperature, to the Triton cryostat [20].

This stage helps cut-off high-frequency peaks due, for example, to mobile phones. The I- and V-lines pass through two Electrolytic Tough Pitch (ETP) copper boxes anchored at the 4K-plate. In each copper box, there are two electrically isolated chips with six RC-filters each, with a common ground at the copper-box.
12 twisted I and V pairs pass through the box and are directly connected to the output Cinch of the box (unfiltered lines), while the other lines are connected to the filters. The motivation for which we use second-order RC-filters rather than

standard RC-stages is related to the needed different degrees of attenuation for the input signal at different frequency-bands.

IAP-plate to MC-plate

At low temperatures and above 10MHz, the RC-filters present losses in attenuation. Thus, we need other filtering stage able to cut-off signals at higher frequencies. To this aim so we installed at the IAP-Plate in the Triton two brass-powder filter stages, both RC-filtered and unfiltered I and V-lines pass through this stage.

A low-pass metal powder filter is an insulated wire surrounded by fine metal grains. The attenuation of high-frequency signals occurs due to the dissipation of current induced in the grains, depending on the powder material, their size, diameter and length of the wire [39][40][41].

In the Triton, we have two rows of 12 insulated manganin (for the voltage lines) and copper wires (for the current lines) with a 0.1mm-diameter, encapsulated in a cylindric paste made of resin, hardener and brass powder. Generally, mixing the powder with epoxies allows us to obtain a better thermalization of the central wire compared with pure powder-made filters [39][40][41]. Both manganin and copper wires are shaped into a spiral, with a distance between the loops of 0.1 mm diameter. The 24 filtered I and V lines terminate with a Cinch connector, which is plugged in the sample holder stage, thermally and mechanically anchored to the bottom of the MC plate. In the sample holder, there is a Cinch-to-Fischer home-made cable of NbTi (for the current lines) and manganin (for the voltage lines), thermalized on the sample holder.

Another problem to take into consideration when studying JJs is the screening of cryostat from the external magnetic field. For this reason, the sample holder is protected by lead and cryoperm screens.
Finally, the characterization of JJs, and in particular of SIs'FS JJs, requires the use of superconducting coils. In the Triton the coil is mechanically anchored to a copper ring centered on the sample stage by means of non-conducting stands. The coil-lines are in copper from the RT-plate to the 4K-plate, and superconducting (NbTi) from the 4K-plate down to the MC. They are thermalized at the 70K-plate, the 4K-plate and at the cold-plate (IAP), and otherwise covered by a fiber glass glove.

3.3 Current-Voltage measurements

In this section, we will deal with the measurement techniques used for most of the characterization in a DC-environment of superconducting systems.

The electronic setup connected to the cryostat allows different measurements useful to characterize different types of devices. All measurements are performed using a four-wire connection useful to exclude all the contributions to the resistance not due to the sample (lines, electrodes, contacts, etc). The junctions are current biased using an Agilent 33120A waveform generator. The generated voltage difference is

applied to a tunable shunt resistance. The frequency of the input signal is low and is always chosen far from 50 Hz in order to avoid resonance effects with electricity grid. The characterization of the junctions have been performed injecting a current with a frequency of $\sim 11Hz$.

In Figure 3.3, it is shown a schematic of the used DC-measurement setup. It is shown that in the system a return current path is provided, which means that it is also possible to measure directly the current passing through the junction.

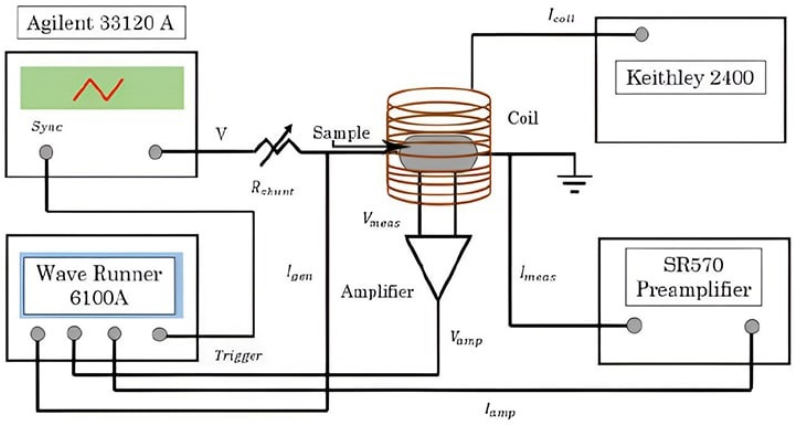

Figure 3.3: Sketch of the used DC setup for current-voltage measurements as a function of the temperature [19].

The recorded output signal is the amplified, by variable gain amplifier battery powered, voltage drop across the junction.

Current versus voltage characteristics can be measured as a function of temperature and/or magnetic field, in order to obtain a wide characterization of the devices.

Due to the complexity of the experimental set-up, the presence of the filtering and amplification stages, electrical and thermal noise effects and the huge number of freedom degrees of a solid state sample strongly affect the results of the experiment. In order to accurately define the properties of the studied junctions the associated errors to the recorded measurements have to be evaluated.
The temperature of the reservoir in which the Josephson junction is thermalized, is registered byan electrical measurement of a diode resistance whose sensitivity at low temperatures is approximately 1×10^{-4} K.
The associated error to the voltage measurements are mainly due to the noise signal because that due to the instruments are negligible compared to the noise. In figure 3.4 is shown a zoom of the noise band of an I-V characteristic of a Josephson junction at a temperature of 2.5K:

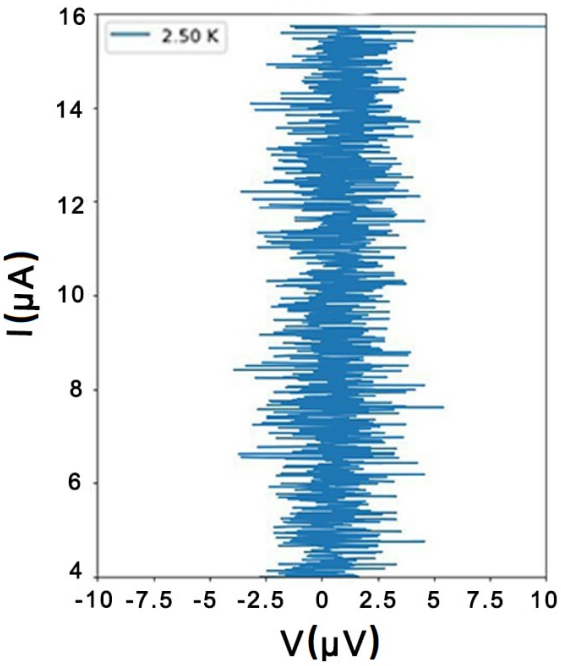

Figure 3.4: Magnification of the superconducting arm of a current-voltage curve at T=2.5K for a Josephson junction Nb based. It shows that the voltage noise amplitude is $4\mu V$ wide.

The width of the voltage noise band is $\Delta V = 4\mu V$ which allows estimating the relative error $\frac{\Delta V}{V}$=1% when a threshold in voltage is fixed for defining the I_c values.

3.3.1 Current-Voltage as a function of the applied magnetic field

The magnetic field parallel to the junction barrier is generated by injecting in a coil a current by Keithley source meter. The error on the generated current is $0.012\% I_{coil}$, as declared in the instrument specifications [42].
We applied a magnetic field from zero to an upper value; after that, the field is swept from a positive value to a negative value, and then goes to zero. For each value of the magnetic field, we acquired the IV characteristics, with a step ΔI_{coil} and till a next field is applied it is waited t=1s. The number of average sweeps for each I-V curve was set to 100.

Chapter 4

Data analysis

In this chapter the transport measurements relative to Nb- and Al-based JJs, of SIs'S and SIs'FS type, will be shown and discussed.
The behavior of the investigated SIs'S JJs follows the theoretical prediction, as derived from the analysis of the I-V curves. This confirms the high quality of the fabricated junctions. Ferromagnetic JJs have been also investigated and show a very high quality since small deviations from the ideal behavior have been recorded, thus confirming their possible use in advanced quantum devices. This conclusion is supported by an analysis of the magnetic response of the junctions.

4.1 Conventional tunnel junctions

Following, it will be discussed the characterization of a SIs'S Josephson junction: Nb(200nm)-AlO_x-Nb(30nm)-Nb(400nm), the numbers in the brackets represent the thickness of the used materials.

4.1.1 Current-Voltage characteristic at base temperature of 10 mK

Figure 4.1 shows the IV characteristic for the SIs'S Josephson junction based on a Niobium technology, at T=10mK.
Former curve was carried out by a current bias given by applying a voltage signal, with a frequency of 1.123 Hz, to a shunt resistor, R_{shunt}=100$K\Omega$.

Figure 4.1 shows an hysteretic behavior of the junction where four different regions are displayed:

- the *superconducting branch* (1) represented by the branch with a finite current and V = 0;
- the *switching branch* (2), represented by the jump from the superconducting arm to the ohmic one (its physical properties go beyond the goal of this thesis and because of that it has been not investigated);
- the *ohmic branch* (3), where IV characteristic shows a linear behavior and allows to extrapolate the normal resistance of the junction;
- the *retrapping branch* (4), related to the process of retrapping of the phase particle into the minima of the washboard potential (see section 1.3.2).

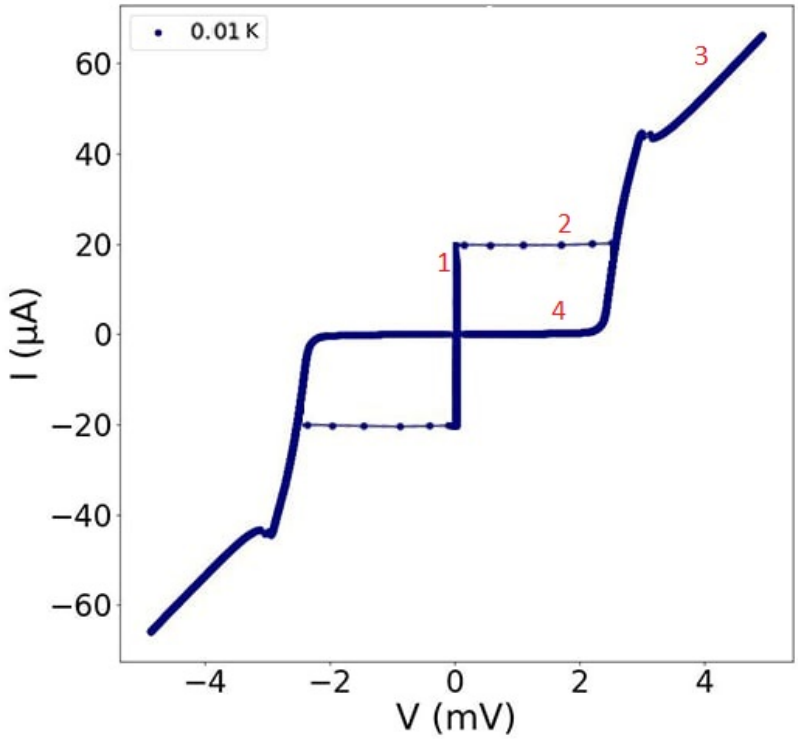

Figure 4.1: IV characteristic for a circular (R=2μm) Josephson junction, based on a Niobium technology, for a SIs'S type: Nb(200nm)-AlO_x-Nb(30nm)-Nb(400nm).

In order to determine the normal resistance R_n or the critical current I_c, and the gap of the junction the IV characteristics were acquired at high current bias. In order to minimize the error that is committed to extrapolate the junction parameters, the data acquisition of IV curves has been split into two data set: at long range (for drops of voltage above $2\Delta/e$), useful to determine the R_n, and those recorded at short range (it defines the part of IV that, from 0 voltage, just shows the phase transition). The former data set allows a better investigation of the critical current of the device. Since the curve in fig. 4.1 shows points having both negative and positive values of I and V, to estimate the I_c it has been adopted the following criterion: $(I_{c_+} + I_{c_-})/2$, where, I_{c_+} and I_{c_-} represent the critical current in the positive and negative of the IV, respectively.

4.1.2 Current-Voltage characteristics as a function of the temperature

Figure 4.2, shows the IV characteristics for a Nb-AlO_x-Nb-Nb junction from 8.8K down to base temperature. At a voltage of the order of a few mV, the characteristics display a resistive branch with a normal resistance $R_n = (69 \pm 2)\Omega$.
At the lowest temperature it shows an hysteretic behavior that disappears while it approaches T_c (critical temperature) and former features can be ascribable to capacitance due to the insulating layer as expected by the RCSJ model [1] [43]. Instead, at high temperatures, the suppression of the hysteric branch is ascribable to the thermal effect and promotes the dissipative effect due to the motion of the quasiparticles of the systems.

Fixing a criterion based on voltage threshold (we choose $V_{Th} \sim 30\mu V$), the critical current (I_c) values, as a function of the temperature, have been extrapolated. The error associated to I_c points has been chosen following the criterion reported in section 3.3.

In figure 4.3, the I_cR_n vs T is shown, and a A.B. type fit was carried out. The data fit has been accomplished using free parameters: the suppression factor (C) and the critical temperature. The suppression factor indicates how much the I_cR_n trend differs from the ideal S-I-S and it represents a quality index for the junction.

We find a good agreement between the theoretical model and the experimental results, having $T_c = (8.5 \pm 0.1)K$ and a suppression factor equal to 0.71 ± 0.01. Former results confirm that the adopted fabrication protocol allows to achieve high quality devices [43].

These results represent the starting point for going towards a bit more complex junctions that, e.g., employing a thin ferromagnetic layer of Py.

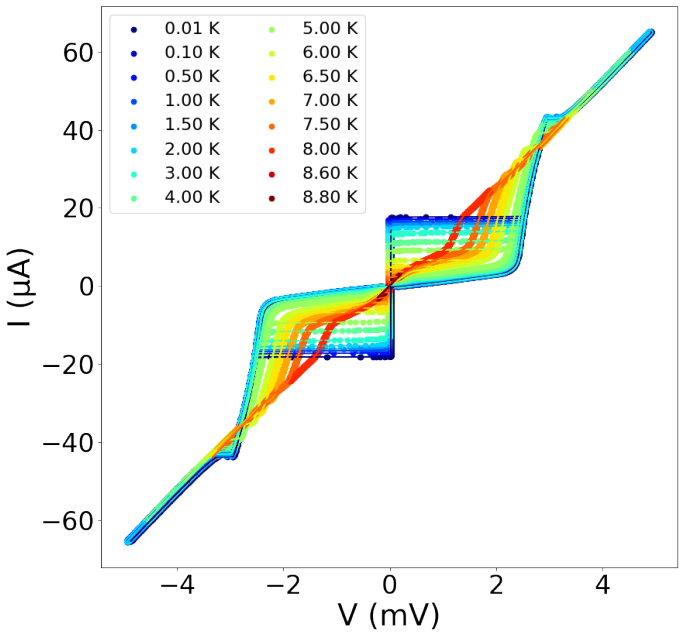

Figure 4.2: Current-Voltage as a function of the temperature for a circular (R=2μm) Josephson junction, of SIs'S type: Nb(200nm)-AlO_x-Nb(30nm)-Nb(400nm).

4.2 SIs'FS based on Nb

Superconducting Josephson junctions employing ferromagnetic materials (SIs'FS JJs) are widely used for making SFQ logic, whose features are low switching energy (about 10^{-9} J/bit at the working temperature of 4.2K) and high switching speed (a few ps/bit) [3]. Following, it will be discussed the characterization of a SIs'FS Josephson junction (Nb(200nm)-AlO_x-Nb(30nm)-Py(3nm)-Nb(400nm)).

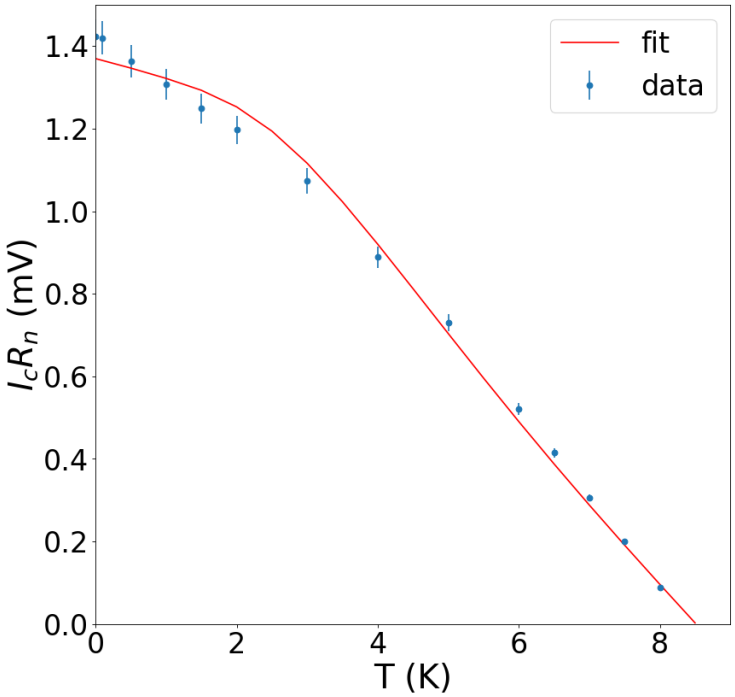

Figure 4.3: I_cR_n vs T for a circular (R=2μm) Josephson junction, based a Niobium technology, of the SIs'S type: Nb(200nm)-AlO_x-Nb(30nm)-Nb(400nm).

4.2.1 Current-Voltage characteristics as a function of the temperature

In figure 4.4, the current-voltage (IV) curves as a function of the temperature from 8K to 10mK for a circular (R=2μm) junction in Nb(200nm)-AlO_x-Nb(30nm)-Py(3nm)-Nb(400nm) architecture are reported. The IV curves show that superconductivity is not completely suppressed in the intermediate Nb layer [44].

Following the procedure described in the previous section, at each value of the temperature, the R_n and I_c values have been extracted.
The obtained R_n is $(187 \pm 4)\Omega$ that gives a specific resistance, R_nA, equal to $(2.3 \pm 0.4) \times 10^3 \Omega\ \mu m^2$. The former values are consistent with those reported in the literature [45].

I_c and R_n as a function of the temperature represent a data set useful to investigate the quality of the JJ, since the Ambegaokar Baratoff model (sec. 1.4.1) allows to evaluate deviations from the ideal behavior of the junction.
The figure 4.5 shows the I_cR_n vs. T plot for the Nb(200nm)-AlO_x-Nb(30nm)-Py(3nm)-Nb(400nm) junction and in red, it is reported, the A.B. theoretical prediction. Through the A.B. fit (equation 1.22) the values of suppression factor C=0.62 ± 0.01 and $T_c = (7.9 \pm 0.1)K$ have been estimated.
Using the estimated suppression factor, we can compare it to the experimental $I_cR_n(0) = (1.26 \pm 0.03)mV$ value having V_{gap}=$(2.7 \pm 0.1)mV$ (defined as the ratio between $4I_cR_n/\pi$C, at T=0).

We need to stress that the A.B. model considers a pure tunnel limit in a S-I-S system, while the investigated junction has additional layers that could lead to a

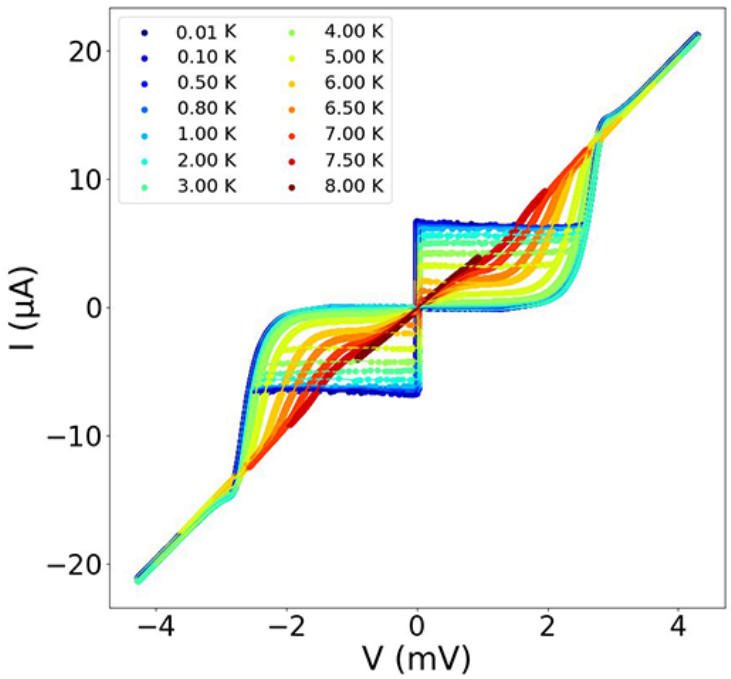

Figure 4.4: Current-Voltage characteristic as a function of the temperature for a circular (R=2μm) Nb(200nm)-AlO_x-Nb(30nm)-Py(3nm)-Nb(400nm) Josephson junction.

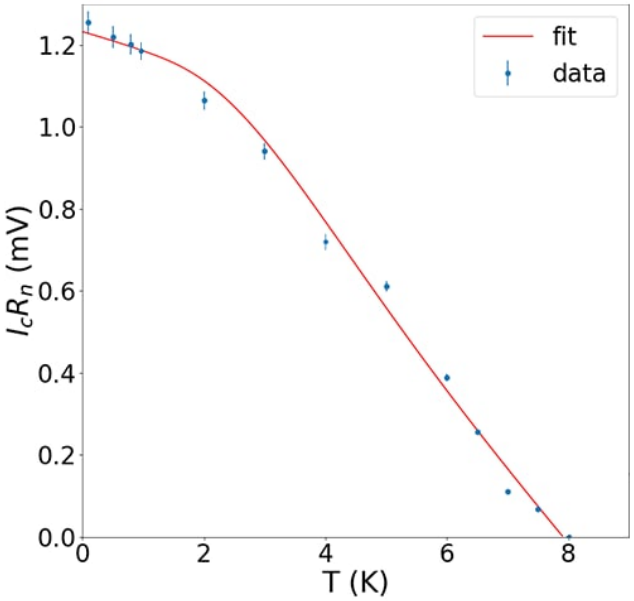

Figure 4.5: Points represent the I_cR_n product as function of the temperature, while in red the Ambegaokar-Baratoff fit curve. The investigation has been carried out for a circular (R=2μm) Nb(200nm)-AlO_x-Nb(30nm)-Py(3nm)-Nb(400nm) junction.

change of behavior of the IV (T) dependence [43]. In the case of junctions made by Niobium, such differences were reported even if there was no additional evaporated normal conducting layer between the superconducting electrodes and the tunneling barrier [16] [43]. This supports the assumption that both a normal layer and a superconducting material weakens the superconducting properties of the junction [43]. Although, there is a deviation in the Ambekaogar-Baratoff model, this procedure gives useful results that allow a better understanding of the fundamental properties

of the junctions and then may support the development of the next generation of SIs'FS junctions.

4.2.2 Comparison between SIs'S and SIs'FS junctions

Following, the comparison between two previously discussed junctions (SIs'S and SIs'FS architecture) will be carried out. Both of them have the same layout (circular JJ, R=2μm) and are based on the Nb technology but differs only with the Py layer.

As reported in figure 4.3, at the lowest temperature, the critical current value is $(20.4 \pm 0.2)\mu A$ and its $R_n = (69 \pm 2)\Omega$, thus allows to estimate $J_c(0) = (160 \pm 20)A/cm^2$, $R_nA = (0.9 \pm 0.1) \times 10^3\Omega\ \mu m^2$ and $I_cR_n(0) = (1.42 \pm 0.04)mV$.
$I_cR_n(0)$ is of the same order of magnitude (mV) of those observed in the presence of the ferromagnetic barrier [44].

When dealing with Josephson junctions of the SFS type, higher critical current values and smaller resistances are observed than those observed in the case of SIs'S Josephson junctions. In order to operate in the SFQ regime, the product I_cR_n must be of the order of 1 mV [28][46]. However, SFS-type junctions are characterized by a product I_cR_n of the order of μV [47], making these junctions incompatible with SFQ logic. The SIs'FS junctions represent a turning point in the SFQ field, as they satisfy the values of the parameters necessary to work in SFQ logic [48], and give the possibility to explore the interactions at the s'/F interface.

Comparing the graphs, in figure 4.3 and 4.5, it can be seen that: in the case of the junction characterized by the presence of a ferromagnetic material, the I_cR_n product is subject to a suppression of 10%, compared to the case without ferromagnet [3]. The suppression of the current is due to the effects at the interface between the s'/F layer, in which Cooper pairs, crossing the barrier, are affected by the exchange field of the ferromagnet [34] [47].

A deep understanding of the properties of the SIs'FS junction can be made by considering the theoretical plot reported in fig.4.6. Bakurskiy et al., in [34], develop a theoretical model useful to predict how the junction behaves by changing the thickness of the ferromagnetic layer. Due to the exchange field, that depends on the domain structures and morphology of the F-layer, the junction deviates from the A.B. trend, even showing a long tail when the temperature approaches T_c [34]. Bakurskiy et al. demonstrate the temperature dependence of theoretical current in the structures with s' thickness around critical one ($L_{Sc} = 3\xi_s$) for different values of exchange field H. These structures are characterized by the existence of the effective critical temperature T_c^* which corresponds to the appearance of superconductivity in middle s-layer and to an exponential growth of the current 4.6.

A further comparison between the two junctions was developed by estimating values of the critical current density, at base temperature and at 4K.
From the literature, it has shown that junctions based on Nb exhibit critical current density values in the range of 50 to 300 A/cm^2 depending on the used oxygen

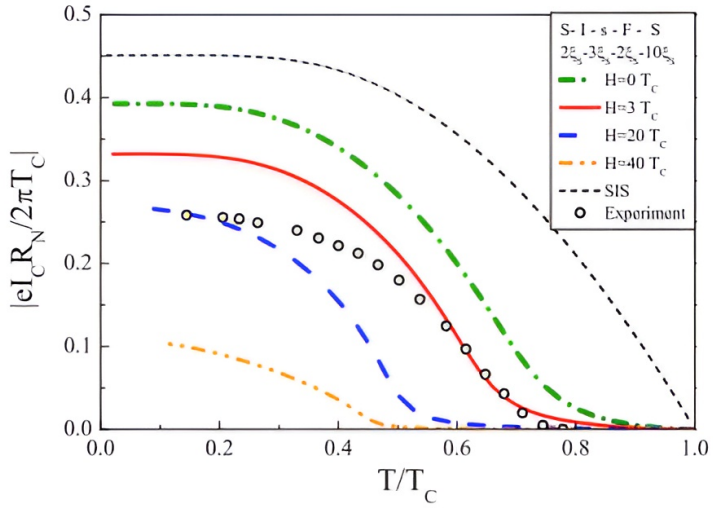

Figure 4.6: The temperature dependence of characteristic voltage I_cR_n of SIsFS structure for different values of exchange field H in the F-layer. Figure adapted from [34].

pressure (9×10^{-7} Pa s to 4×10^{-5} Pa s) useful for building the insulating barrier [49]. In the case of the analyzed junctions, it can be observed how the presence of the ferromagnet leads to a suppression of the value of the critical current density (J_c) that at base temperature assumes values of (160 ± 20) A/cm^2, in absence of ferromagnet, while in presence of ferromagnet it is (53 ± 8) A/cm^2 [50]. At 4K, $J_c = (100 \pm 10) A/cm^2$ for SIs'FS and $J_c = (33 \pm 5)$ A/cm^2 for a junction without a ferromagnetic layer.

4.3 Magneto-transport properties: IVH

Following, the characterization in presence of magnetic field, for the investigated SIs'S and SIs'FS JJs.

4.3.1 SIs'S Josephson junction

By applying a current to a superconducting coil, a magnetic field is generated, then the superconducting properties of the junction are recorded. The magnetic field has been swept in both direction (negative and positive values) recording, at base temperature, IV curves that we called "up" and "down", respectively. For each recored dataset, following the same procedure shown in the previous section, the I_c values are extrapolated and shown as a function of the magnetic filed, in figure 4.7.

Since the junction under investigation has a circular geometry, as reported in the theoretical chapter, its critical current dependence on the applied magnetic field follows the Airy relation (sec. 1.4.2), that allows to estimate the junction parameters, like the radius and the London penetration depth λ_L.
Using the relation 4.1, parameters such as $R = (2.1 \pm 0.2)\mu m$, $\lambda_L = (100 \pm 3) nm$ have been estimated and the obtained values are compatible with others found in

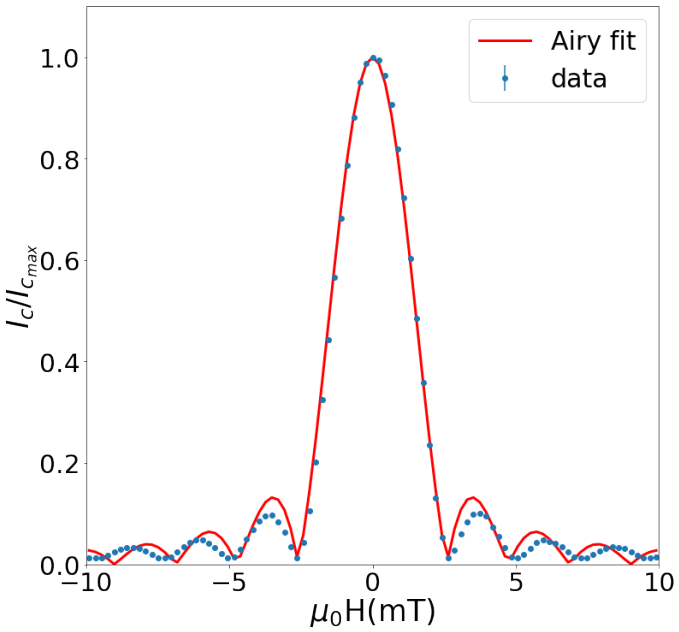

Figure 4.7: The scattered points represent the experimental data of $I_c(H)$ characteristic for a circular (R=2μm) Josephson junction of the SIs'S type: Nb(200nm)-AlO_x-Nb(30nm)-Nb(400nm) while red line represents the curve predicted by Airy model.

literature [51][52].

$$\frac{I_c}{I_{c_{max}}}(H;R,d) = \left| 2\frac{J_1(\frac{\pi\phi}{\phi_0})}{\frac{\pi\phi}{\phi_0}} \right| \tag{4.1}$$

with $\phi = 2HRd$, and ϕ_0 =2.07 mA pH, where R corresponds to the radius of the junction, and $d = 2\lambda_S + d_{ox}$, to the length of magnetic penetration.

Since the red fit line reported in fig. 4.7 well fit the experimental data, it manifests a good uniformity of the current distribution in the junction [51][52].

4.3.2 SIs'FS Josephson junction

We have also investigated the magnetic response of a SIs'FS junction where the thickness of the intermediate superconducting layer s' is kept fixed at 30nm and a thin layer of Py, 3nm thick, has been deposited.
In figure 4.8 the I_c-H dependence is shown at T=6K. It exhibits, as expected for JJs employing a thin ferromagnetic layer, an hysteretic behavior of the I_c(H) [3]. In agreement with what has been discussed in section 1.6.3 and 1.7.1, two patterns are shifted depending on whether increasing or decreasing magnetic fields are sent to the junction. The shift between the two patterns makes these junctions available as RAM (random access memories) [3] [53] [54].

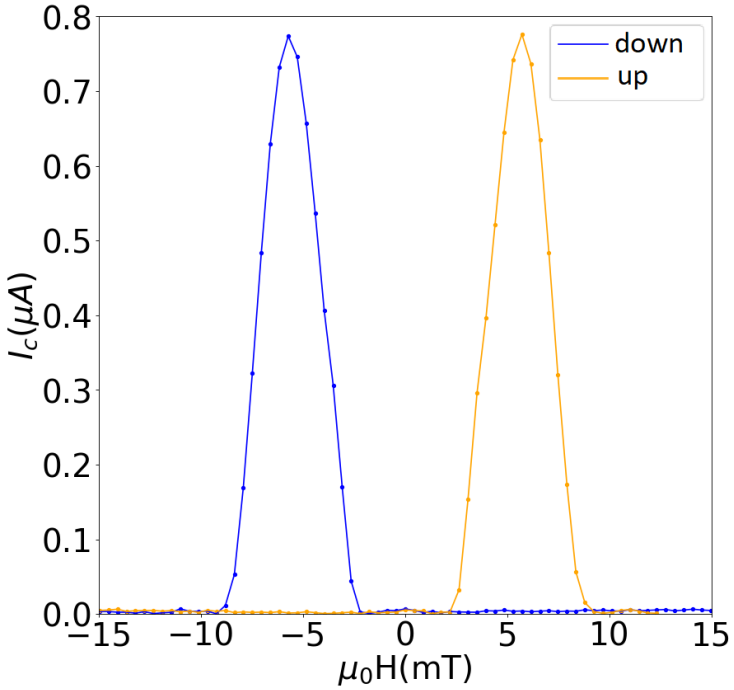

Figure 4.8: The scattered points of the I_c vs H curve concern the experimental data per for a circular (R=2μm) Nb(200nm)-AlO_x-Nb(30nm)-Py(3nm)-Nb(400nm) junction at T=6K, while the fill lines represents the fit by Airy model.

4.4 Transport properties for SIs'FS with s' 10nm thick

In this section, we will discuss the IV curve for a circular ($R = 1\mu m$) SIs'FS JJ made using Nb and employing a thin ferromagnetic layer, with a thickness s' layer fixed to $d_{s'}$=10nm. The IV curves are reported in figure 4.9.

Following the same procedure described in the previous section both R_n and I_c values have been extrapolated from the I-V curves. The I_cR_n product as a function of the temperature, for SIs'FS junction, is shown in figure 4.10.

As reported by Bakurskiy et al. [34], the behavior of the junction is strongly influenced by the thickness of the s'-interlayer, and the I_cR_n curve does not follow the A.B. prediction. At the lowest T it shows a plateau, while at high T (for $T \sim T_c$) a tail of I_cR_n curve is displayed with an exponential dependence on the temperature. Former trend is typical for junctions in which the transport properties are ruled by the proximity effect, where the new length of scale ξ_n - that depends on the normal properties of the s' layer - defines the decay length scale [1] [16] [21]. At intermediate temperatures, the tail could be still interpreted in terms of proximity effect, since ξ_n increases its value by reducing the temperature and even the exponential decay changes its trend[16].
This I_cR_n behavior is due to the fact that when a SIs'FS junction has the thickness of s' comparable to the correlation length of the superconductor, it ceases to behave like an SIs' + s'FS series [33] [34]. Conversely, proximity effects prevail and the junction behaves like an SInFS JJ [34].

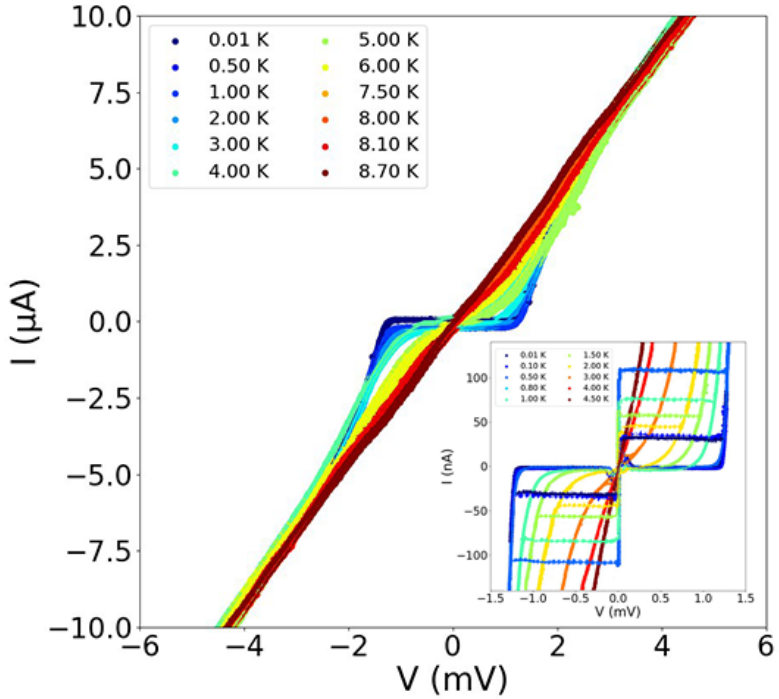

Figure 4.9: IV characteristic for a circular (R=1 μm) Josephson junction, based on a Niobium technology, of the SIs'FS type: Nb(200nm)-AlO_x-Nb(10nm)-Py(3nm)-Nb(400nm). In the box, the magnification of the IV curves shows the hysterical nature at low temperature, for the recorded data.

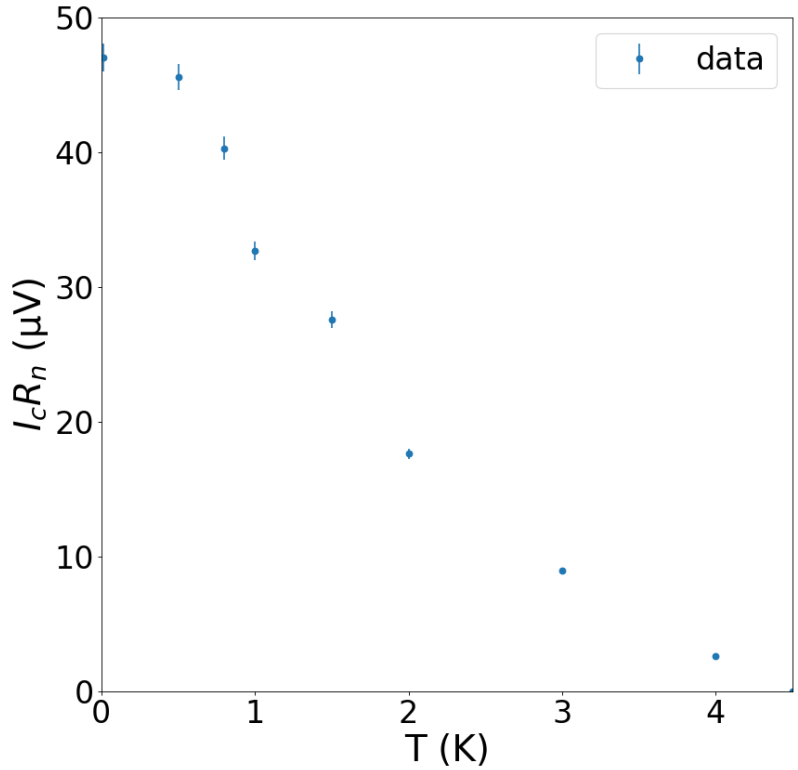

Figure 4.10: I_cR_n product for a circular (R=1 μm) Nb(200nm)-AlOx- Nb(10nm)-Py(3nm)-Nb(400nm) Josephson junction.

A comparison between I_cR_n values for SIs'FS junctions having different thicknesses

for the s' layer (10 and 30nm) has been carried out and the results are summarized in table 4.1. It can be observed that the junction having s' layer, $d_{s'} = 10nm$ shows a reduction of about two orders of magnitude of the $I_cR_n(0)$ product, equal to $(47 \pm 1)\mu V$, respect to the thicker junction.

	SIs'FS JJ	SIs'FS JJ
$d_{s'}(nm)$	30	10
R (μm)	2	1
$J_c(0)$ (A/cm^2)	53 ± 8	3.5 ± 0.5
$R_n(\Omega)$	187 ± 4	420 ± 8
$I_cR_n(0)(mV)$	1.26±0.03	0.047 ± 0.001

Table 4.1: The table shows the characteristic values of $J_c(0)$, R_n, $I_cR_n(0)$ for the two SIs'FS junctions, with different thickness of the s' layer. Values of $J_c(0)$, R_n, $I_cR_n(0)$ represent the critical current density, the normal resistance and the critical current normal resistance product, respectively.

4.5 SIs'FS based on Al

In this section the transport measurements of Josephson junctions based on Al and employing a thin ferromagnetic layer will be shown. They will be investigated by transport measurements, as a function of the temperature and of the applied magnetic field, and represent the first type of Josephson junctions that combine the Al technology with ferromagnetic materials [35] [55].

4.5.1 IV characteristics as a function of the temperature

In figure 4.11 the current-voltage characteristics as a function of the temperature IV(T) for the junctions Al(200nm)- AlOx-Al(30nm)-Al(350nm) (SIs'S) and Al(200nm)- AlOx-Al(30nm)-Py(3nm)-Al(350nm) (SIs'FS) are shown.
The curves are recorded in the range of temperature from 1.3K down to 10mK. At lowest temperature they show an hysteretic behavior, thus confirming their underdamped transport regime (see 1.3.2) while a complete phase transition at the normal state, for temperature above 1.3K, is shown.

Performing the procedure explained in the former sections, the normal resistance R_n of the junctions under investigations have been estimated. For SIs'S and SIs'FS junctions, we find $R_n = (1.7 \pm 0.7) \times 10^3\Omega$ and R_n=$(1.8 \pm 0.7) \times 10^3\Omega$, respectively. Even their specific resistance has been evaluated as the product between the normal resistance and their cross section, finding $R_nA = (21 \pm 3) \times 10^3\Omega\mu m^2$ for SIs'S and $R_nA = (23 \pm 3) \times 10^3\Omega\mu m^2$ for SIs'FS architecture [35].

By IVT curves, reported in figure 4.11, and fixing a voltage threshold of the order of tens micron-volts, the values of I_c as a function of the temperature have been extrapolated.

Josephson junctions based on Aluminum technology show a critical current of the

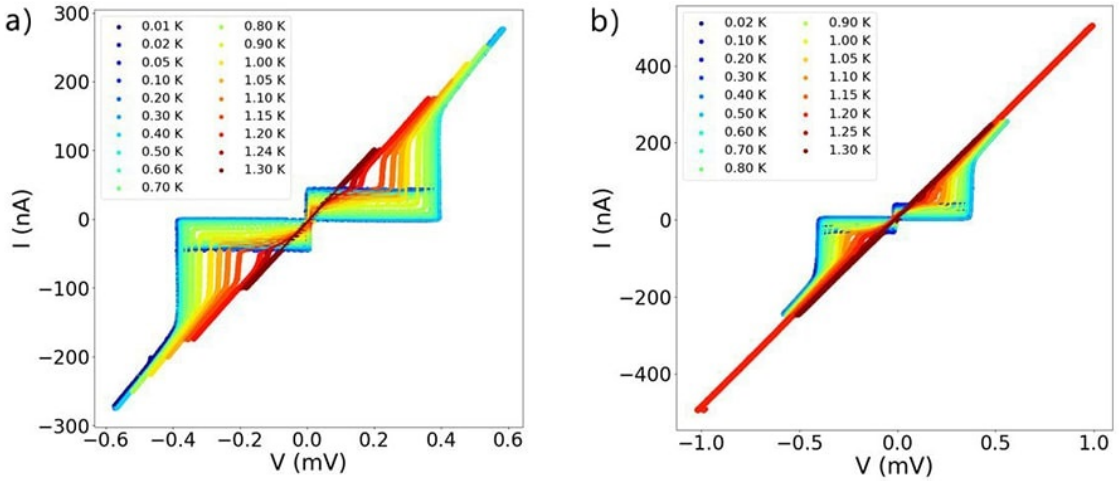

Figure 4.11: The figure shows the IV(T) characteristics for two circular (R=2 μm) Josephson junctions based on Aluminium in (a) SIs'S and (b)SIs'FS architecture.

order of tens of nano-Ampere (three orders of magnitude lower than that of the Nb JJs). These small amplitude for I_c are strongly affected by any noise sources. Because of that, the associated error to I_c has been estimated as difference between I_{c_-} and I_{c_+}. More challenging the estimation of I_c is when the temperature approaches T_c since the already reduced I_c amplitude becomes comparable to the experimental resolution. In order to make a better valuation near T_c it is necessary to perform an RCSJ fit [1], but, in this analysis, we are interested in temperature values below T_c, and for this reason it has not been performed [1].

We find that, at base temperature, for the SIs'S JJ $I_c(0) = (44 \pm 2)nA$, while for the SIs'FS JJ $I_c(0) = (42 \pm 1)nA$; former values are compatible with those reported in litterature in the tunnel limit [35] [56].

In figure 4.12, the scattered points represent the I_cR_n product as function of the temperature T for: a) SIs'S and b) SIs'FS junctions; the red line represents the prediction by A.B. model.
The extrapolated parameters, and the characteristic voltage $I_cR_n(0)$, for both the junctions, are summarized in table 4.2.

Comparing the previous data with those collected with Nb-based junctions, greater compatibility is observed between the experimental data of I_cR_n and the A.B. model [35], due to a thin natural AlO_x barrier that decouples the Al from the ferromagnetic layer - eliminating the exchange coupling at their interface - and the Al layer that does not experience any exchange field.
Previous studies, on the tunneling conductance of junctions consisting of a thin Al films coupled to semiconducting ferromagnetic layers of materials, such as EuO and EuS, confirm our achieved results [57] [58].

Further investigations on the mechanisms that play an important rule of tuning the properties at interface between the Al and ferromagnetic materials are still needed

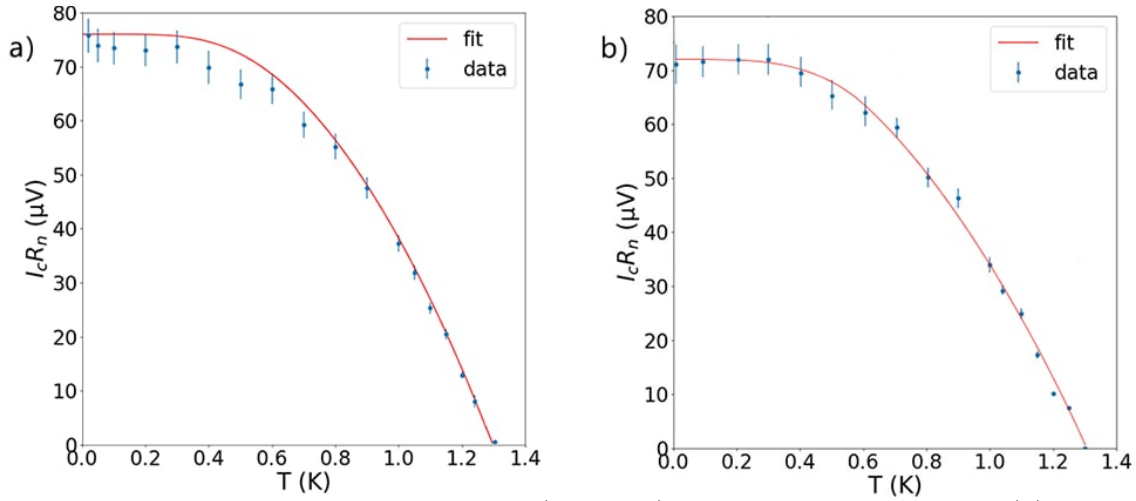

Figure 4.12: I_cR_n product for circular (R=2μm) Josephson junctions in (a) SIs'S type and (b) SIs'FS type.

and a next generation of devices and experiments are currently under development.

	SIs'S JJ	SIs'FS JJ
$T_c(K)$	1.29 ± 0.01	1.30 ± 0.02
C	0.22 ± 0.02	0.27 ± 0.03
$I_cR_n(0)$ (μV)	76 ± 3	72 ± 3

Table 4.2: It summarizes the extrapolated values, $T_c(K)$ and C, and the experimental $I_cR_n(0)$ for SIs'S and SIs'FS JJs, based on Aluminium.

4.5.2 IV measurements as a function of the magnetic field

In this section, it will be reported on the magnetic characterization of the superconducting junctions. The experimental data are then compared with the theoretical models described in the first chapter.

SIs'S Josephson junction

The properties of the superconducting junction based on Al technology have been investigated.
In figure 4.13 its magnetic pattern at T=10mK is shown. Blue scattered points represent the experimental data that have been extrapolated by current-voltage curves recorded meanwhile the applied magnetic field (H) is swept from H_{min} to H_{max}.
Since the investigated Al based junction has a circular geometry, the magnetic dependence of the experimental data has been fitted by using the Airy model.
The red curve shows a good agreement between the theoretical prediction and the recorded data, thus confirming the high quality of the tunnel barrier for the junction. The data fitting procedure has allowed to have the estimate R=$(1.6 \pm 0.4)\mu m$ and λ_L=(30±2) nm (values in agreement with those reported in literature [59]).

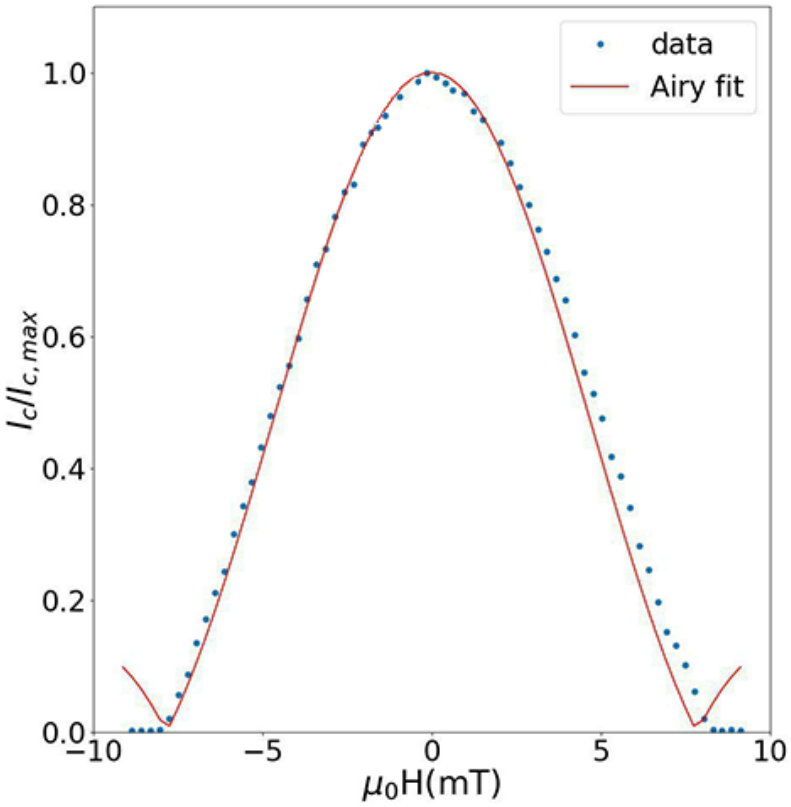

Figure 4.13: It shows the $I_c/I_{c_{max}}$ vs. the applied magnetic field at T=10mK, for a circular (R=2μm) SIs'S Josephson junction based on Al.

SIs'FS Josephson junction

In this section the magnetic dependence of the critical current (I_c vs. H) for the SIs'FS junction made with Al will be discussed. The figure 4.14 shows the I_c vs. H curves at T=10mK. The scattered points represent the experimental data.

As it is discussed in [34], due to the thinner s' layer, the junction work as a series of two junctions: SIs' and s'FS. Since the critical current $I_{c_{SIs'}} \ll I_{c_{s'FS}}$, the entire junction will works as a S-I-S JJ, and its I_c-H dependence will still follow the Airy expression 1.28, where the flux quantum Φ_0 will include terms that depend on the London penetration depth and the concentration of the magnetic clusters in the F layer oriented parallel or antiparallel to the applied magnetic field [34] . Airy patterns are expected to be shifted to a point where the flux due to the external field cancels out the flux due to the magnetization. Specifically, when H is ramped from positive to negative fields, the Airy-like pattern is shifted toward negative fields because of the positive remanence of the F layer, whereas when H is ramped from negative to positive fields, the pattern is shifted toward positive fields.

Al based Josephson junctions employing a thin ferromagnetic layer that have been investigated in this thesis represent the state of the art of switchable and low dissipative quantum devices. Due to their properties, this junctions represent the key element of future advanced architecture for the quantum computation.

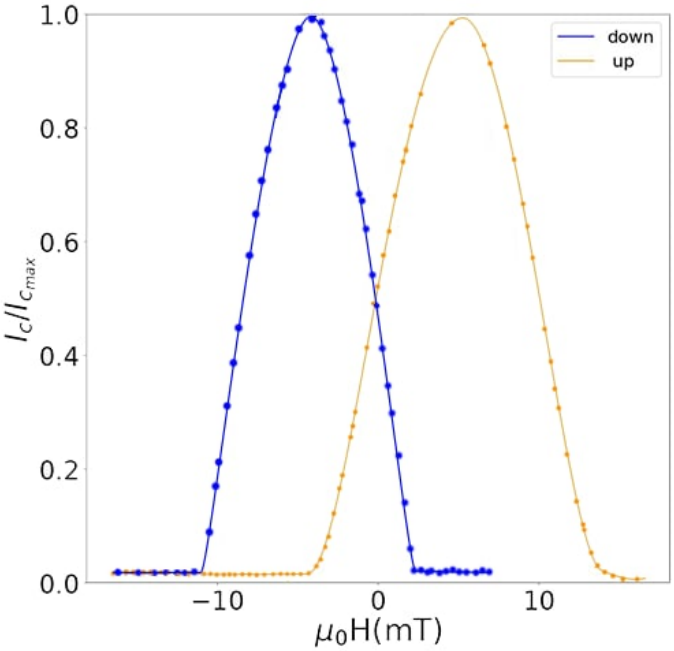

Figure 4.14: Experimental dependence of $I_c/I_{c_{max}}$ versus increasing (blue) and decreasing (yellow) external magnetic field, for circular (R=2μm) Al Josephson junction employing a thin ferromagnetic layer.

In table 4.3 the main parameters of the junctions based on Al and Nb in SIs'FS and SIs'S architecture are summarized.

JJ	Tech.	$d_{s'}$ (nm)	R (μm)	T_c(K)	$J_c(0)$ (A/cm^2)	$I_cR_n(0)$ (mV)
SIs'S	Nb	30	2	8.5 ± 0.1	160 ± 20	1.42 ± 0.04
SIs'FS	Nb	30	2	7.9 ± 0.1	53 ± 8	1.26 ± 0.03
SIs'FS	Nb	10	1	4.5 ± 0.5	3.5 ± 0.5	0.047 ± 0.001
SIs'S	Al	30	2	1.29 ± 0.01	0.35 ± 0.01	0.076 ± 0.003
SIs'FS	Al	30	2	1.30 ± 0.02	0.33 ± 0.05	0.072 ± 0.003

Table 4.3: It summarizes the main parameters for Al and Nb based junctions investigated in this thesis.

Conclusion

In this thesis work, junctions in SIs'S and SIs'FS (S represents a superconducting layer of Al or Nb, s' a thin layer of superconductor, I an insulating barrier while F a thin ferromagnetic - Permalloy - material) architectures have been investigated. These devices have been fabricated by combining deposition and microfabrication techniques. Up to now ferromagnetic JJs have been only fabricated using Nb or NbN as superconductors, in view of applications as memories or as components of classical superconducting electronics [30] [44] [60]. This is one of the first studies in which a ferromagnet is integrated in an Al JJ with the prespective of being used in a variety of quantum circuits. The sizes of the junctions are micrometrics and they have a circular geometry with a radius R=2μm. I contributed to the characterization of the junctions by cryogenic magneto-transport measurements down to 10mK. The recorded current-voltage measurements have been useful to compare the experimental data with the Ambegaokar-Baratoff model. This analysis has allowed to achieve information about the quality of the barrier in both SIs'S and SIs'FS architectures with Al and Nb and even to investigate the regime in which the system evolves [34]. Junctions based on Al employing a thin ferromagnetic layer, have been fabricated and characterized, and represent devices, at the state of the art, where the superconducting characteristics of Al and that magnetic of the Permalloy are for the first time integrated [35]. Due to their micrometric size and to the critical current, at base temperature, of the order of tens of nano-Ampere, junctions based on the Al material open up to advanced circuits for the quantum computation, circumventing the more advanced and expensive techniques useful for shrinking down to nanoscale the sizes of the junctions. Former makes easily accessible the regime in which the Josephson energy $E_j \sim I_c$ has to be larger than the charge energy $E_c \sim 1/C$ (C represents the capacitance of the system) but smaller enough ($I_c \sim$ tens nA) to be measurable with our experimental set up (4-8 GHz). These results pave the way to the investigation of the fundamental properties of the SIs'S that could be employed in new architectures of qu-bit made by coupling superconducting resonant circuits with ferromagnetic junction. The presence of the F-layer, is an extra knob for the junction. Thus representing a new degree of the freedom for the new generation of Trasmon qu-bit devices (called by Ahmad et a. "Ferro-Trasmon" [61]).

Appendix A

Appendix

A.1 BCS Theory

A.1.1 Landau Fermi-liquid

For a system of Fermions, the ground state corresponds to the filled states with energies E below the maximal Fermi energy E_F, while the excitations are created by moving a particle from a state below the Fermi surface to a state above it.
We can imagine this process as the superposition of the removal of a particle of a state below the Fermi surface and the addition of a particle to a state above the Fermi surface.
We increase the energy of the system by taking a particle out of the state with an energy $E_1 < E_F$ and create a hole excitation with a positive energy $\epsilon_1 = E_F - E_1$, or, by adding a particle with an energy $E_2 > E_F$ and create a hole excitation with a positive energy $\epsilon_2 = E_2 - E_F$.
Let us define the Hamiltonian for particles and holes:

$$\hat{H}_e = \frac{1}{2m}\left(-i\hbar\nabla - \frac{e}{c}\vec{A}\right)^2 + U(\vec{r}) - \mu \tag{A.1}$$

where μ is the chemical potential and $U(\vec{r})$ is the potential energy.
The wave function of a particle excitation $u_{\epsilon,\vec{p}}(\vec{r})$ with an energy ϵ and momentum $\vec{p}$ satisfies

$$\hat{H}_e u_{\epsilon,\vec{p}}(\vec{r}) = \epsilon_{\vec{p}} u_{\epsilon,\vec{p}}(\vec{r}). \tag{A.2}$$

The hole wave function $v_{\epsilon,\vec{p}}(\vec{r})$ with an energy ϵ and momentum $\vec{p}$ satisfies

$$\hat{H}_h v_{\epsilon,\vec{p}}(\vec{r}) = \epsilon_{\vec{p}} v_{\epsilon,\vec{p}}(\vec{r}), \tag{A.3}$$

where an hole excitation is the absence of a particle with the energy $-\epsilon$ and momentum $-\vec{p}$.
What we get is:

$$\hat{H}_h = -\hat{H}_e^* \tag{A.4}$$

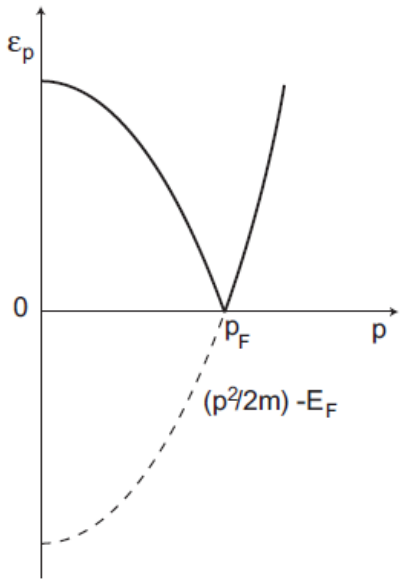

Figure A.1: Single-particle spectrum (dashed line) in transformed into Landau excitation spectrum in a strongly correlated Fermi liquid (solid line).

A.1.2 The Cooper problem

Consider two electrons above a filled Fermi sphere. The electrons are united by the the exchange of phonons, and have opposite spins and opposite momenta.
Their wave functions are $u_{\vec{p}} = e^{i\vec{p}\cdot\vec{r}}U_{\vec{p}}$ and $u_{\vec{-p}} = e^{-i\vec{p}\cdot\vec{r}}U_{-\vec{p}}$.
The pair wave function is

$$\Psi_{\vec{p}}^{pair}(\vec{r}_1,\vec{r}_2) = u_p(\vec{r}_1)u_{-\vec{p}}(\vec{r}_2) = e^{i\frac{\vec{p}\cdot(\vec{r}_1-\vec{r}_2)}{\hbar}}U_{\vec{p}}V_p^* \tag{A.5}$$

We carry out a linear combination of the moment:

$$\Psi_{\vec{p}}^{pair}(\vec{r}_1,\vec{r}_2) = \sum e^{i\frac{\vec{p}\cdot(\vec{r}_1-\vec{r}_2)}{\hbar}}a_{\vec{p}} \tag{A.6}$$

where $a_{\vec{p}} = U_{\vec{p}}V_{\vec{p}}^*$.
The inverse transformation is

$$a_{\vec{p}} = V^{-1}\int \Psi(\vec{r})e^{\frac{i\vec{p}\vec{r}}{\hbar}}d^3r \tag{A.7}$$

where V is the volume of the system.
In this way the Schroedinger equation has the form

$$\left[\hat{H}_e(\vec{r}_1) + \hat{H}_e(\vec{r}_2) + W(\vec{r}_1,\vec{r}_2)\right]\Psi^{pair}(\vec{r}_1,\vec{r}_2) = E\Psi^{pair}(\vec{r}_1,\vec{r}_2) \tag{A.8}$$

multiplying by $e^{-i\vec{p}(\vec{r}_1-\vec{r}_2)}$ we obtain

$$[2\epsilon_{\vec{p}} - E_{\vec{p}}]a_{\vec{p}} = -\sum W_{\vec{p},\vec{p}_1}a_{\vec{p}_1} \tag{A.9}$$

where

$$W_{\vec{p},\vec{p}_1} = \begin{cases} \frac{W}{V}, \epsilon_{\vec{p}} \text{ and } \epsilon_{\vec{p}_1} < E_c \\ 0, \epsilon_{\vec{p}} \text{ and } \epsilon_{\vec{p}_1} > E_C \end{cases} \tag{A.10}$$

where $E_c << E_F$.
We obtain

$$a_{\vec{p}} = \frac{W}{E - 2\epsilon_{\vec{p}}} \frac{1}{V} \sum a_{\vec{p}_1} = \frac{W}{E - 2\epsilon_{\vec{p}}} \sum{}' a_{\vec{p}_1} \tag{A.11}$$

that give us

$$\frac{1}{W} = \sum{}' \frac{1}{E - 2\epsilon_{\vec{p}}} \tag{A.12}$$

For an attraction W<0 we have

$$\frac{1}{|W|} = \sum{}' \frac{1}{2\epsilon_{\vec{p}} - E} = N(0) ln\Big(\frac{|E_0| + 2E_c}{|E_0|}\Big) \tag{A.13}$$

that yields:

$$|E_0| = \frac{2E_C}{e^{\frac{1}{N(0)|W|}} - 1} \tag{A.14}$$

We see that exists a state of a particle-hole pair with an energy below the Fermi surface.

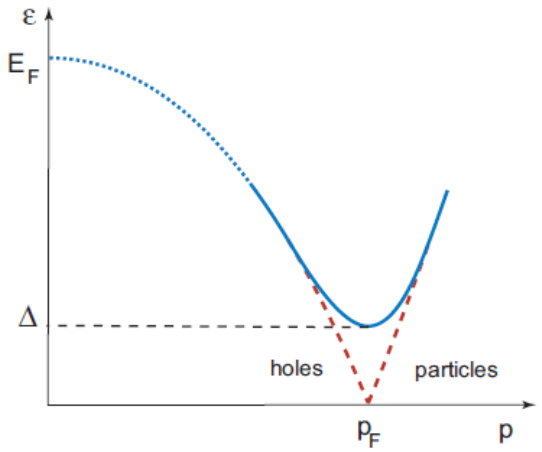

Figure A.2: The coupling between electron and hole modifies the energy spectrum. A gap opens up near the Fermi surface.

A gap opens up near the Fermi surface.

A.1.3 The Bogoliubov-de Gennes equations

Coupling between particles and holes is described by introduction of pairing field Δ into the particle and hole equations.
The resulting equations are

$$\hat{H}_e u(\vec{r}) + \Delta(\vec{r}) v(\vec{r}) = \epsilon u(\vec{r}) \tag{A.15}$$

$$-\hat{H}_e^* v(\vec{r}) + \Delta^*(\vec{r}) u(\vec{r}) = \epsilon v(\vec{r}) \tag{A.16}$$

The functions (u,v) are orthogonal

$$\int [u_m^*(\vec{r}) u_n(\vec{r}) + v_m^*(\vec{r}) v_n(\vec{r})] d^3r = \delta_{m,n} \tag{A.17}$$

If we consider the case where $\nabla = |\nabla| e^{i\chi}$ is costant in space, and the magnetic field is absent.

$$\Big[-\frac{\hbar^2}{2m}\nabla^2 - \mu \Big] u(\vec{r}) + \Delta v(\vec{r}) = \epsilon u(\vec{r}) \tag{A.18}$$

$$\Big[-\frac{\hbar^2}{2m}\nabla^2 - \mu \Big] v(\vec{r}) + \Delta^* u(\vec{r}) = \epsilon v(\vec{r}) \tag{A.19}$$

where $\mu = \frac{\hbar^2 K_F^2}{2m}$. We look for a solution in the form

$$u = e^{\frac{i}{2}\chi} U_{\vec{q}} e^{i\vec{q}\cdot\vec{r}} \tag{A.20}$$

$$v = e^{-\frac{i}{2}\chi} V_{\vec{q}} e^{i\vec{q}\cdot\vec{r}} \tag{A.21}$$

In this way

$$\xi_{\vec{q}} U_{\vec{q}} + |\Delta| V_{\vec{q}} = \epsilon_{\vec{q}} U_{\vec{q}} \tag{A.22}$$

$$-\xi_{\vec{q}} V_{\vec{q}} + |\Delta| U_{\vec{q}} = \epsilon_{\vec{q}} V_{\vec{q}} \tag{A.23}$$

with $\xi_{\vec{q}} = \frac{\hbar^2}{2m}\Big[q^2 - k_F^2\Big]$.

The solution is

$$\epsilon_{\vec{q}} = \pm\sqrt{\xi_{\vec{q}^2} + |\Delta|^2} \tag{A.24}$$

where we consider only energies $\epsilon > 0$.

$$U_{\vec{q}} = \frac{1}{\sqrt{2}}\Big(1 + \frac{\xi_{\vec{q}}}{\epsilon_{\vec{q}}}\Big)^{\frac{1}{2}} \tag{A.25}$$

$$V_{\vec{q}} = \frac{1}{\sqrt{2}}\Big(1 - \frac{\xi_{\vec{q}}}{\epsilon_{\vec{q}}}\Big)^{\frac{1}{2}} \tag{A.26}$$

$|\Delta|$ is the lowest single-particle excitation energy in the superconducting state, while $2|\Delta|$ is the energy which is needed to destroy the Cooper pair.

A.2 Feymann derivation

According to the Ginzburg-Landau theory, we can describe a superconductor through a macroscopic wave function.
Starting from the Ginzburg-Landau theory and the Schroedinger equation I want to derive the Josephson equations.

Let consider a Josephson junction, the macroscopic wave function thar describes each superconductor is:
$\Psi_1 = \sqrt{n_1} e^{i\phi_1}$ and $\Psi_2 = \sqrt{n_2} e^{i\phi_2}$.
We substitute the two functions within the Schroedinger equation:

$$i\hbar\frac{\partial \Psi_1}{\partial t} = U\Psi_1 - K\Psi_2 \tag{A.27}$$

and

$$i\hbar\frac{\partial\Psi_2}{\partial t} = U\Psi_2 - K\Psi_1 \tag{A.28}$$

where U is the potential to which the material is subject, and K describes the link between the superconductors.
Explicit Ψ:

$$i\hbar\frac{\partial\sqrt{n_1}e^{i\phi_1}}{\partial t} = U_1\sqrt{n_1}e^{i\phi_1} - K\sqrt{n_2}e^{i\phi_2} \tag{A.29}$$

$$i\hbar\frac{\partial\sqrt{n_2}e^{i\phi_1}}{\partial t} = U_2\sqrt{n_2}e^{i\phi_2} - K\sqrt{n_1}e^{i\phi_1} \tag{A.30}$$

multiplying by $e^{(-i\phi_1)}and e^{(i\phi_2)}$, we have:

$$i\hbar\frac{1}{2\sqrt{n_1}}\frac{\partial n_1}{\partial t} - \hbar\sqrt{n_1}\frac{\partial\phi_1}{\partial t} = U_1\sqrt{n_1} - K\sqrt{n_2}e^{-i(\phi_1-\phi_2)} \tag{A.31}$$

$$i\hbar\frac{1}{2\sqrt{n_2}}\frac{\partial n_2}{\partial t} - \hbar\sqrt{n_2}\frac{\partial\phi_2}{\partial t} = U_2\sqrt{n_2} - K\sqrt{n_1}e^{i(\phi_2-\phi_1)} \tag{A.32}$$

We assume $|U_1| = |U_2| = qV$ and we separate the real part from the imaginary one.

For the real part we get:

$$\frac{\partial\phi_1}{\partial t} = -\frac{qV}{2\hbar} + \frac{K}{\hbar}\sqrt{\frac{n_2}{n_1}}\cos\phi \tag{A.33}$$

$$\frac{\partial\phi_2}{\partial t} = \frac{qV}{2\hbar} + \frac{K}{\hbar}\sqrt{\frac{n_1}{n_2}}\cos\phi \tag{A.34}$$

We subtract them and derive the second Josephson equation:

$$\frac{\partial\phi}{\partial t} = \frac{2eV}{\hbar} \tag{A.35}$$

Instead, for the imaginary part:

$$\frac{\partial n_2}{\partial t} = \frac{2K}{\hbar}\sqrt{n_2 n_1}\sin\phi \tag{A.36}$$

$$\frac{\partial n_1}{\partial t} = -\frac{2K}{\hbar}\sqrt{n_2 n_1}\sin\phi \tag{A.37}$$

For $\vec{J} = -q\frac{\partial n}{\partial t}$ we obtain the second Josephson equation:

$$I = I_c\sin\phi \tag{A.38}$$

A.3 Andreev reflection

In 1964, Andreev demonstrated how the single electron state of the normal metal can be converted into Cooper pairs, and explained how the electrical current at the interface can turn into a dissipationless current. An electron, in a normal state material is reflected at the interface as a hole, and produces a Cooper pair in the superconductor. So the normal current in N is converted to a supercurrent in S, and

a charge 2e across the interface is transferred, as shown in A.3 [22].

An electron of the normal metal affects the S/N interface, with energy lower than that of the superconducting gap, it carries with it an electron of the valence band with energy -ϵ. In this way a Cooper pair will form inside the superconductor and an electron hole-pair inside the metal: the hole-electron pair will have information about the superconducting state of S, while electrons that form the Cooper pair have moment k_F+dk and -k_F+dk respectively, total moment will be equal to 2dk <<k_F. This implies a spatial modulation of the order parameter of 2dk within a ξ_N correlation length.

Assume that both the normal metal and the superconductor have the same Fermi velocity, there are no insulating barriers between them, and the gap varies over distances longer than the electron wave length k_F^{-1}. Consider a particle incident from the normal region on the superconducting half-space $x > 0$, with a momentum parallel to the x axis, and assume that the magnetic field is absent [22].

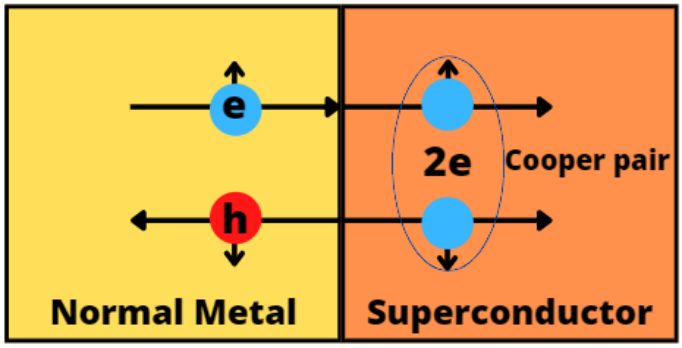

Figure A.3: Rapresentation of Andreev reflection. In this case an electron arrives at the interface and becomes a Cooper pair.

When $\epsilon > |\Delta|$, the particle will penetrate into the superconductor and partially will be reflected back into the normal metal.
So the wave functions that will describe this process will be:

$$\begin{pmatrix} u \\ v \end{pmatrix}_L = e^{i(k_x + \frac{\epsilon}{\hbar v_x}x + ik_y y + ik_z z)} \begin{pmatrix} 1 \\ 0 \end{pmatrix} + ae^{i(k_x - \frac{\epsilon}{\hbar v_x}x + ik_y y + ik_z z)} \begin{pmatrix} 0 \\ 1 \end{pmatrix} \tag{A.39}$$

where the first term correspond to an incident particle, while the second term to a reflected hole.
The wave function on the right describes a transmitted particle will have the form:

$$\begin{pmatrix} u \\ v \end{pmatrix}_R = ce^{i(k_x + \lambda_S)x + ik_y y + ik_z z} \begin{pmatrix} U_0 \\ V_0 \end{pmatrix} \tag{A.40}$$

with

$$\lambda_S = \frac{\sqrt{\epsilon^2 - |\Delta|^2}}{\hbar v_x} \tag{A.41}$$

and

$$U_0 = \frac{1}{\sqrt{2}}\left[1 + \frac{\sqrt{\epsilon^2 - |\Delta|^2}}{\epsilon}\right]^{\frac{1}{2}} \text{ and } V_0 = \frac{1}{\sqrt{2}}\left[1 - \frac{\sqrt{\epsilon^2 - |\Delta|^2}}{\epsilon}\right]^{\frac{1}{2}}$$

If we consider that $a = \frac{V_0}{U_0}$, a describes the process when a particle is reflected as a hole from a spatially non uniform gap.

If the energy is $\epsilon < |\Delta|$, the wave function on the right is:

$$\begin{pmatrix} u \\ v \end{pmatrix}_R = ce^{i(k_x + \tilde{\lambda_S})x + ik_y y + ik_z z} \begin{pmatrix} \tilde{U}_0 \\ \tilde{V}_0 \end{pmatrix} \tag{A.42}$$

where

$$\tilde{\lambda}_S = \frac{\sqrt{\epsilon^2 - |\Delta|^2}}{\hbar v_x} \tag{A.43}$$

and

$$a = \frac{U_0}{V_0} \qquad\qquad |a|^2 = 1$$

the Andreev reflection is complete since there are no transmitted particles.

$I_S(\phi)$ can be written in terms of the occupied Andreev bound states energies ϵ_n:

$$I_\phi = -\frac{e}{\hbar} \sum_{\epsilon<0} \frac{\partial \epsilon(\psi)}{\phi} \tanh\left(\frac{\epsilon_n}{2k_b T}\right). \tag{A.44}$$

Where the Andreev levels within the energy gap region directly depend on the energy gap Δ and the trasparency of the barrier [26] [1].

Bibliography

[1] F. Tafuri. *Fundamentals and Frontiers of the Josephson Effect*. Springer Series in Materials Science. Springer International Publishing, 2019. ISBN: 9783030207267. URL: https://books.google.it/books?id=6gqwDwAAQBAJ.

[2] Igor I. Soloviev et al. In: *Beilstein Journal of Nanotechnology* 8 (2017), "2689–2710". ISSN: "2190-4286". DOI: "10.3762/bjnano.8.269".

[3] Loredana Parlato et al. "Characterization of scalable Josephson memory element containing a strong ferromagnet". In: *Journal of Applied Physics* 127.19 (2020), p. 193901. DOI: 10.1063/5.0004554. eprint: https://doi.org/10.1063/5.0004554. URL: https://doi.org/10.1063/5.0004554.

[4] Yuki Ando et al. "Design and Demonstration of an 8-bit Bit-Serial RSFQ Microprocessor: CORE e4". In: *IEEE Transactions on Applied Superconductivity* 26.5 (2016), pp. 1–5. DOI: 10.1109/TASC.2016.2565609.

[5] Timofei I. Larkin et al. "Ferromagnetic Josephson switching device with high characteristic voltage". In: *Applied Physics Letters* 100.22 (2012), p. 222601. DOI: 10.1063/1.4723576. eprint: https://doi.org/10.1063/1.4723576. URL: https://doi.org/10.1063/1.4723576.

[6] J. Bardeen, L. N. Cooper, and J. R. Schrieffer. "Theory of Superconductivity". In: *Phys. Rev.* 108 (5 Dec. 1957), pp. 1175–1204. DOI: 10.1103/PhysRev.108.1175. URL: https://link.aps.org/doi/10.1103/PhysRev.108.1175.

[7] M. Tinkham. *Introduction to Superconductivity*. International series in pure and applied physics. McGraw Hill, 1996. ISBN: 9780070648784. URL: https://books.google.it/books?id=XP_uAAAAMAAJ.

[8] L.D. Landau et al. *Electrodynamics of Continuous Media*. COURSE OF THEORETICAL PHYSICS. Elsevier Science, 2013. ISBN: 9781483293752. URL: https://books.google.it/books?id=jedbAwAAQBAJ.

[9] P. Muller et al. *The Physics of Superconductors: Introduction to Fundamentals and Applications*. Springer Berlin Heidelberg, 2010. ISBN: 9783642082511. URL: https://books.google.it/books?id=vg2McgAACAAJ.

[10] URL: https://publications.lib.chalmers.se/records/fulltext/234640/234640.pdf.

[11] A. Barone and G. Paterno. *Physics and Applications of the Josephson Effect*. A Wiley-interscience publication. Wiley, 1982. ISBN: 9780471014690. URL: https://books.google.it/books?id=FrjvAAAAMAAJ.

[12] Raffaella Ferraiuolo. "Master Thesis: Fabbricazione e caratterizzazione comparativa di nanostrutture superconduttive, Universita degli studi di Napoli, Federico II. (2019/2020)". MA thesis.

[13] Rupert L. Frank et al. "Microscopic derivation of Ginzburg-Landau theory." In: *Journal of the American Mathematical Society* 25.3 (2012), pp. 667–713. ISSN: 08940347, 10886834. URL: http://www.jstor.org/stable/23265088 (visited on 10/06/2022).

[14] P.M. Chaikin and T.C. Lubensky. *Principles of Condensed Matter Physics*. Cambridge University Press, 2000. ISBN: 9780521794503. URL: https://books.google.it/books?id=P9YjNjzr9OIC.

[15] Annette Bussmann-Holder and Hugo Keller. "High-temperature superconductors: underlying physics and applications". In: *Zeitschrift für Naturforschung B* 75.1-2 (Oct. 2019), pp. 3–14. DOI: 10.1515/znb-2019-0103. URL: https://doi.org/10.1515$%5C%$2Fznb-2019-0103.

[16] K. K. Likharev. "Superconducting weak links". In: *Rev. Mod. Phys.* 51 (1 Jan. 1979), pp. 101–159. DOI: 10.1103/RevModPhys.51.101. URL: https://link.aps.org/doi/10.1103/RevModPhys.51.101.

[17] E. Burstein. *Tunneling Phenomena in Solids: Lectures presented at the 1967/NATO Advanced Study Institute at Risö, Denmark*. Springer US, 2012. ISBN: 9781468417524. URL: https://books.google.it/books?id=4RgDCAAAQBAJ.

[18] Halima Giovanna Ahmad. "Master thesis: Physics of the Josephson effect in junctions with ferromagnetic barriers". MA thesis. 2016/2017.

[19] Roberta Satariano. "Master Thesis: Eterostrutture per lo sviluppo di memorie criogeniche". MA thesis.

[20] Halima Giovanna Ahmad. "PhD thesis: Physics of the Josephson effect in junctions with ferromagnetic barriers towards quantum circuits and RF applications". PhD thesis. 2021.

[21] A. A. Golubov and M. Yu. Kupriyanov. "The current phase relation in Josephson tunnel junctions". In: *Journal of Experimental and Theoretical Physics Letters* 81.7 (Apr. 2005), pp. 335–341. DOI: 10.1134/1.1944074. URL: https://doi.org/10.1134$%5C%$2F1.1944074.

[22] A. I. Buzdin. "Proximity effects in superconductor-ferromagnet heterostructures". In: *Rev. Mod. Phys.* 77 (3 Sept. 2005), pp. 935–976. DOI: 10.1103/RevModPhys.77.935. URL: https://link.aps.org/doi/10.1103/RevModPhys.77.935.

[23] Samme M. Dahir, Anatoly F. Volkov, and Ilya M. Eremin. "Phase-dependent spin polarization of Cooper pairs in magnetic Josephson junctions". In: *Phys. Rev. B* 100 (13 Oct. 2019), p. 134513. DOI: 10.1103/PhysRevB.100.134513. URL: https://link.aps.org/doi/10.1103/PhysRevB.100.134513.

[24] A. S. Vasenko et al. "Properties of tunnel Josephson junctions with a ferromagnetic interlayer". In: *Physical Review B* 77.13 (Apr. 2008). DOI: 10.1103/physrevb.77.134507. URL: https://doi.org/10.1103$%5C%$2Fphysrevb.77.134507.

[25] G. Grosso and G.P. Parravicini. *Solid State Physics*. Elsevier Science, 2000. ISBN: 9780080481029. URL: https://books.google.it/books?id=L5RrQbbvWn8C.

[26] D. S. Rabinovich et al. "Resistive State of Superconductor-Ferromagnet-Superconductor Josephson Junctions in the Presence of Moving Domain Walls". In: *Phys. Rev. Lett.* 123 (20 Nov. 2019), p. 207001. DOI: 10.1103/PhysRevLett.123.207001. URL: https://link.aps.org/doi/10.1103/PhysRevLett.123.207001.

[27] R. Caruso et al. "RF assisted switching in magnetic Josephson junctions". In: *Journal of Applied Physics* 123.13 (2018), p. 133901. DOI: 10.1063/1.5018854. eprint: https://doi.org/10.1063/1.5018854. URL: https://doi.org/10.1063/1.5018854.

[28] V. V. Bol'ginov et al. "Magnetic switches based on Nb-PdFe-Nb Josephson junctions with a magnetically soft ferromagnetic interlayer". In: *Soviet Journal of Experimental and Theoretical Physics Letters* 95.7 (June 2012), pp. 366–371. DOI: 10.1134/S0021364012070028.

[29] Bethany M Niedzielski et al. "S/F/S Josephson junctions with single-domain ferromagnets for memory applications". In: *Superconductor Science and Technology* 28.8 (July 2015), p. 085012. DOI: 10.1088/0953-2048/28/8/085012. URL: https://doi.org/10.1088/0953-2048/28/8/085012.

[30] Roberta Satariano et al. "Inverse magnetic hysteresis of the Josephson supercurrent: Study of the magnetic properties of thin niobium/permalloy interfaces". In: *Physical Review B* 103.22 (June 2021). DOI: 10.1103/physrevb.103.224521. URL: https://doi.org/10.1103$%5C%$2Fphysrevb.103.224521.

[31] S. V. Bakurskiy et al. "Theory of supercurrent transport in SIsFS Josephson junctions". In: *Physical Review B* 88.14 (Oct. 2013). DOI: 10.1103/physrevb.88.144519. URL: https://doi.org/10.1103$%5C%$2Fphysrevb.88.144519.

[32] S. V. Bakurskiy et al. "Theoretical model of superconducting spintronic SIsFS devices". In: *Applied Physics Letters* 102.19 (2013), p. 192603. DOI: 10.1063/1.4805032. eprint: https://doi.org/10.1063/1.4805032. URL: https://doi.org/10.1063/1.4805032.

[33] Igor V. Vernik et al. "Magnetic Josephson Junctions With Superconducting Interlayer for Cryogenic Memory". In: *IEEE Transactions on Applied Superconductivity* 23.3 (2013), pp. 1701208–1701208. DOI: 10.1109/TASC.2012.2233270.

[34] S. V. Bakurskiy et al. "Theoretical model of superconducting spintronic SIsFS devices". In: *Applied Physics Letters* 102.19 (2013), p. 192603. DOI: 10.1063/1.4805032. eprint: https://doi.org/10.1063/1.4805032. URL: https://doi.org/10.1063/1.4805032.

[35] A. Vettoliere et al. "Aluminum-ferromagnetic Josephson tunnel junctions for high quality magnetic switching devices". In: *Applied Physics Letters* 120.26 (2022), p. 262601. DOI: 10.1063/5.0101686. eprint: https://doi.org/10.1063/5.0101686. URL: https://doi.org/10.1063/5.0101686.

[36] I. A. Golovchanskiy et al. "Magnetization dynamics in dilute Pd1-xFex thin films and patterned microstructures considered for superconducting electronics". In: *Journal of Applied Physics* 120.16 (2016), p. 163902. DOI: 10.1063/1.4965991. eprint: https://doi.org/10.1063/1.4965991. URL: https://doi.org/10.1063/1.4965991.

[37] Alessandro Gaggero. "Thesis entitled: Rivelatori di singolo fotone a nanofili superconduttori". In: *Universita degli studi Roma Tre (Italy)* (20-Gen-2010).

[38] URL: https://pdf.medicalexpo.com/pdf/oxford-instruments/triton/100694-213183.html.

[39] John M. Martinis, Michel H. Devoret, and John Clarke. "Experimental tests for the quantum behavior of a macroscopic degree of freedom: The phase difference across a Josephson junction". In: *Phys. Rev. B* 35 (10 Apr. 1987), pp. 4682–4698. DOI: 10.1103/PhysRevB.35.4682. URL: https://link.aps.org/doi/10.1103/PhysRevB.35.4682.

[40] F. P. Milliken et al. "50 Ω characteristic impedance low-pass metal powder filters". In: *Review of Scientific Instruments* 78.2 (2007), p. 024701. DOI: 10.1063/1.2431770. eprint: https://doi.org/10.1063/1.2431770. URL: https://doi.org/10.1063/1.2431770.

[41] A. Lukashenko and A. V. Ustinov. "Improved powder filters for qubit measurements". In: *Review of Scientific Instruments* 79.1 (2008), p. 014701. DOI: 10.1063/1.2827515. eprint: https://doi.org/10.1063/1.2827515. URL: https://doi.org/10.1063/1.2827515.

[42] Mark A Cejer et al. "Choosing the optimal source measurement unit instrument for your test and measurement application". In: *Source measure unit* (2013). URL: https://assets.testequity.com/te1/Documents/ARTICLE_LIBRARY/Keithley-Choosing$%5C%$20the$%5C%$20Optimal$%5C%$20Source$%5C%$20Measurement$%5C%$20Unit$%5C%$20Instrument$%5C%$20for$%5C%$Your$%5C%$20Test$%5C%$20and$%5C%$20Measurement$%5C%$20Application.pdf.

[43] P. Seidel and J. Richter. "Theoretical Investigation of the Critical Josephson Current of Niobium-Lead Tunnel Junctions". In: *physica status solidi (b)* 99.2 (1980), pp. 607–613. DOI: https://doi.org/10.1002/pssb.2220990220. eprint: https://onlinelibrary.wiley.com/doi/pdf/10.1002/pssb.2220990220. URL: https://onlinelibrary.wiley.com/doi/abs/10.1002/pssb.2220990220.

[44] R. Caruso et al. "RF assisted switching in magnetic Josephson junctions". In: *Journal of Applied Physics* 123.13 (2018), p. 133901. DOI: 10.1063/1.5018854. eprint: https://doi.org/10.1063/1.5018854. URL: https://doi.org/10.1063/1.5018854.

[45] H. Safa et al. "Specific Resistance Measurement of a Single Grain Boundary in Pure Niobium". In: *Proc. SRF'99* (Santa Fe, NM, USA, Nov. 1999). JACoW Publishing, Geneva, Switzerland, pp. 267–269. URL: https://jacow.org/SRF99/papers/TUP029.pdf.

[46] Burm Baek et al. "Hybrid superconducting-magnetic memory device using competing order parameters". In: *Nature Communications* 5.1 (May 2014). DOI: 10.1038/ncomms4888. URL: https://doi.org/10.1038$%5C%$2Fncomms4888.

[47] Tairzhan Karabassov et al. "Anomalous current-voltage characteristics of SFIFS Josephson junctions with weak ferromagnetic interlayers". In: *Beilstein Journal of Nanotechnology* 11 (Jan. 2020), pp. 252–262. DOI: 10.3762/bjnano.11.19. URL: https://doi.org/10.3762$%5C%$2Fbjnano.11.19.

[48] S. V. Bakurskiy et al. "Protected 0-pi states in SIsFS junctions for Josephson memory and logic". In: *Applied Physics Letters* 113.8 (Aug. 2018), p. 082602. DOI: 10.1063/1.5045490. URL: https://doi.org/10.1063$%5C%$2F1.5045490.

[49] C. Granata et al. "Integrated LTc-SQUID magnetometers for multichannel systems". In: *IEEE Transactions on Applied Superconductivity* 11.1 (2001), pp. 95–98. DOI: 10.1109/77.919293.

[50] Alan W. Kleinsasser, Ronald E. Miller, and William H. Mallison. "Dependence of critical current density on oxygen exposure in Nb-AlO(x)-Nb tunnel junctions". In: *IEEE Transactions on Applied Superconductivity* 5.1 (Mar. 1995), pp. 26–30. DOI: 10.1109/77.384565.

[51] O. M. Kapran et al. "Crossover between short- and long-range proximity effects in superconductor/ferromagnet/superconductor junctions with Ni-based ferromagnets". In: *Phys. Rev. B* 103 (9 Mar. 2021), p. 094509. DOI: 10.1103/PhysRevB.103.094509. URL: https://link.aps.org/doi/10.1103/PhysRevB.103.094509.

[52] A. I. Gubin et al. "Dependence of magnetic penetration depth on the thickness of superconducting Nb thin films". In: *Phys. Rev. B* 72 (6 Aug. 2005), p. 064503. DOI: 10.1103/PhysRevB.72.064503. URL: https://link.aps.org/doi/10.1103/PhysRevB.72.064503.

[53] Valeriy Ryazanov et al. "Magnetic Josephson Junction Technology for Digital and Memory Applications". In: *Physics Procedia* 36 (Dec. 2012), pp. 35–41. DOI: 10.1016/j.phpro.2012.06.126.

[54] I. Vaskivskyi et al. "Fast electronic resistance switching involving hidden charge density wave states". In: *Nature Communications* 7.1 (May 2016). DOI: 10.1038/ncomms11442. URL: https://doi.org/10.1038$%5C%$2Fncomms11442.

[55] A. Jouan et al. "Josephson junctions via anodization of epitaxial Al on an InAs heterostructure". In: *Applied Physics Letters* 119.17 (2021), p. 172601. DOI: 10.1063/5.0060757. eprint: https://doi.org/10.1063/5.0060757. URL: https://doi.org/10.1063/5.0060757.

[56] P. Santhanam et al. "Resistance anomaly near the superconducting transition temperature in short aluminum wires". In: *Phys. Rev. Lett.* 66 (17 Apr. 1991), pp. 2254–2257. DOI: 10.1103/PhysRevLett.66.2254. URL: https://link.aps.org/doi/10.1103/PhysRevLett.66.2254.

[57] X. Hao, J. S. Moodera, and R. Meservey. "Spin-filter effect of ferromagnetic europium sulfide tunnel barriers". In: *Phys. Rev. B* 42 (13 Nov. 1990), pp. 8235–8243. DOI: 10.1103/PhysRevB.42.8235. URL: https://link.aps.org/doi/10.1103/PhysRevB.42.8235.

[58] Guo-Xing Miao et al. "Spin regulation in composite spin-filter barrier devices". In: *Nature communications* 5 (2014), p. 3682. ISSN: 2041-1723. DOI: 10.1038/ncomms4682. URL: https://doi.org/10.1038/ncomms4682.

[59] Katrin Steinberg, Marc Scheffler, and Martin Dressel. "Quasiparticle response of superconducting aluminum to electromagnetic radiation". In: *Phys. Rev. B* 77 (21 June 2008), p. 214517. DOI: 10.1103/PhysRevB.77.214517. URL: https://link.aps.org/doi/10.1103/PhysRevB.77.214517.

[60] Hirotaka Terai and Zhen Wang. "Fabrication of NBN single flux quantum (SFQ) circuit and operating properties at 10 K". In: *Electronics and Communications in Japan (Part II: Electronics)* 84 (Oct. 2001), pp. 34–39. DOI: 10.1002/ecjb.1063.

[61] Halima Giovanna Ahmad et al. "Hybrid ferromagnetic transmon qubit: Circuit design, feasibility, and detection protocols for magnetic fluctuations". In: *Physical Review B* 105.21 (June 2022). DOI: 10.1103/physrevb.105.214522. URL: https://doi.org/10.1103$%5C%$2Fphysrevb.105.214522.